Physics – Uspekhi **65** (2) 111 – 130 (2022)

REVIEWS OF TOPICAL PROBLEMS PACS numbers: 78.20.Bh, 78.30.Fs, 78.66.Li, **78.67.–n**, 78.67.De

Localized excitons and trions in semiconductor nanosystems

M A Semina, R A Suris

DOI: https://doi.org/10.3367/UFNe.2020.11.038867

Contents

Abstract. The optical properties of semiconductors and nanoheterostructures based on them are determined near the fundamental absorption edge by electron–hole complexes such as excitons and charged three-particle complexes, aka trions. We present the results of theoretical studies of the structure and binding energies of localized excitons and trions in nanosystems within the variational approach. This approach is applicable to a wide range of semiconducting systems, from quantum wells, wires, and dots based on classical group III–V and II–VI semiconductors to van der Waals heterostructures made of monolayers of transition-metal dichalcogenides. We also discuss many-particle effects in structures containing resident charge carriers. Our treatment of theoretical approaches is accompanied by a discussion of extensive experimental results available in the literature.

Keywords: exciton, trion, binding energy, wave function, localization, quantum well, monolayer of transition-metal dichalcogenides, variational method, optical spectrum

1. Introduction

The history of the study of electron–hole complexes in condensed matter dates back to the 1930s. The existence of excitons — bound complexes of an electron and a hole in solids — was predicted by Frenkel in 1931 [1, 2]. In those papers, attention was drawn to the fact that the absorption of light in a crystal may not be accompanied by an increase in conductivity if the photoexcited carriers form a bound state. In his studies, Frenkel discussed molecular crystals, in which the excitation at one site freely propagates along the crystal lattice. Such excitons are called small-radius, or Frenkel, excitons.

In most semiconductors, charge carriers are weakly bound to lattice sites. They can form hydrogen-like electron–hole complexes, also called Wannier–Mott excitons (large-radius excitons). Such complexes were predicted by Wannier [3] in 1937, and their theory was later developed by Mott in 1938 [4]. Large-radius excitons were first observed experimentally in 1951 in copper oxide by Gross and Karryev [5]. This started intensive experimental and theoretical studies of excitons. By the early 1960s, a theory of excitons in ideal crystals was constructed, the applicability limits of the Frenkel and Wannier models were identified, intermediate-radius excitons were considered [6], a theory of light absorption in solids was constructed taking the exciton effects into account, and the study of the participation of excitons in transport phenomena was begun [7].

The possibility of the existence of bound three-particle electron–hole complexes in semiconductors was predicted in 1958 by Lampert [8]. Such complexes are called trions, or charged excitons. Similar quantum mechanical systems made of two identical particles and a third particle with a different mass and opposite electric charge are the hydrogen ion H^- (corresponding to an X^- trion) and the molecular ion H_2^+ (corresponding to an X^+ trion). The H^- and H_2^+ ions were first studied theoretically in the late 1920s [9, 10]. The main difference between trions and the H^- and H_2^+ ions is that the mass ratio of an electron and a hole is no longer a small

M A Semina, R A Suris
Ioffe Institute,
ul. Politekhnicheskaya 26, 194021 St. Petersburg, Russian Federation
E-mail: msemina@gmail.com, suris.theory@mail.ioffe.ru

Received 18 August 2020, revised 14 November 2020
Uspekhi Fizicheskikh Nauk **192** (2) 121 – 142 (2022)
Translated by S Alekseev

quantity. From the theoretical standpoint, this does not allow separating the coordinates of the electron and hole subsystems, which makes the calculations much more complicated. The stability of both types of trions for an arbitrary ratio of the effective masses of the electron and the hole was proved theoretically in the late 1970s [11–13]. The binding energy of trions in bulk materials is extremely low, equal to several hundredths of the bulk exciton energy [13, 14], which does not allow reliable experimental observations of trions in bulk materials [15–17].

Increasing interest in the study of electron–hole complexes is related to the development of technology for the synthesis of low-dimensional semiconducting heterostructures. One of the main effects of reducing the system dimension is a considerable enhancement of the interaction between particles, which leads to a significant increase in the binding energy of such complexes. For example, in passing from a bulk semiconductor to an ideal two-dimensional quantum well, the exciton binding energy increases by a factor of four [18], while the trion binding energies can increase by almost an order of magnitude [19–21]. The first experimental observations of an X^- trion were made in 1992 by Heng et al. on a CdTe-based quantum well structure [22]. X^+ trions were discovered a few years later, in 1996 [23].

The binding energy of electron–hole complexes increases even more strongly in moving to quantum wires. For example, the binding energy of an exciton [24, 25] and both types of trions [26–28] in quasi-one-dimensional systems with a finite barrier can exceed the binding energy of the corresponding ideal two-dimensional complexes by a factor of two or more. The X^- trion was first observed experimentally in a quantum wire in 2002 [29], and the X^+ trion, in 2005 [28]. Electron–hole complexes are also actively studied in carbon nanotubes (see, e.g., [30–34]) and quantum dot structures (see, e.g., [35–37]), where their binding energy also significantly exceeds those in bulk systems.

In the last two decades, the physics of nanostructures has been enriched by a new class of two-dimensional systems, two-dimensional crystals: primarily graphene, monolayers of boron nitride, two-dimensional black phosphorus, and monomolecular layers of transition-metal dichalcogenides. The last are described by the chemical formula MX_2 (where M is a transition metal, usually Mo or W, and X is a chalcogen, most commonly, S, Se, or Te). Transition-metal dichalcogenide monolayers hold promise for applications in electronics and optoelectronics, because these systems are direct-gap semiconductors with the band gap $E_g \approx 2$ eV [38–43]. Currently, there are ample opportunities to produce van der Waals heterostructures in which monolayers of transition-metal dichalcogenides, graphene, and other two-dimensional semiconductors are interspersed with hexagonal boron nitride, which provides tunnel-impenetrable barriers and significantly improves the optical properties of such systems [44]. From the standpoint of optical spectroscopy, the key features of MX_2 monolayers and the van der Waals heterostructures based on them are the extremely strong Coulomb interaction effects [45–47]. In particular, the binding energy of an exciton reaches several hundred meV, and that of a trion, tens of meV. Thus, excitons and trions dominate the optical response of transition-metal dichalcogenides [48, 49].

The problem of finding the energy spectrum and wave functions of Coulomb complexes turns out to be very nontrivial. Its exact analytic solution is possible only for an exciton in the simplest particular cases of a hydrogen-like complex in three-dimensional and two-dimensional systems. Even the model problem of an exciton in a quantum wire structure can no longer be solved in the general form due to the unavailability of the one-dimensional limit in the Coulomb problem. Two-dimensional systems based on transition-metal dichalcogenides have a sufficiently high dielectric contrast, and hence the interparticle interaction potential differs significantly from the Coulomb one, which also makes the corresponding problem impossible to solve analytically. Currently, two strategies can be adopted in the theory of Coulomb complexes. The first is based on numerical calculations, including numerical diagonalization of the Hamiltonian of the electron–hole complex [50, 51], and variational methods using trial functions with a large (of the order of 10^4) number of fitting parameters. Such methods are most efficient for calculating structures with specific parameters. The second strategy is to use simple but physically substantiated trial functions with a small number of fitting parameters, which, albeit at the cost of some decrease in accuracy, allows obtaining a physically transparent picture of the structure of excitons and trions.

Because trions are excited in doped structures, the question of correlations between photoexcited complexes and the Fermi sea of charge carriers is important [52]. The problem of excitons and exciton complexes in semiconductors with a small but finite concentration of free charge carriers is extremely challenging, because the ground state of a low-density electron gas (with the Fermi energy comparable to the Coulomb repulsion energy) cannot be determined analytically [53]. Attempts have been made to follow the evolution of the exciton binding energy with an increase in the density of free electrons, taking the Hartree–Fock corrections due to the electron–electron interaction into account and using the orthogonality of the exciton wave functions to the occupied Fermi-sea states (the corresponding calculations for quantum wells are given, e.g., in [54–56]). The dependence of the absorption spectrum on the electron concentration was measured experimentally, for example, in [57]. At high electron gas concentrations, an asymmetric peak is observed; as the concentration decreases, it evolves into a set of maxima corresponding to the exciton and trions.

The purpose of this article is to review the variational methods developed in the last two decades for the analysis of Coulomb complexes in nanosystems, based on the use of simple and physically substantiated trial functions, and to describe the general patterns of evolution of their binding energies and structure depending on the dimension of the system and the presence of additional localization of charge carriers. In the last section, we discuss the question of correlations between the photoproduced excitons and the Fermi sea of charge carriers in doped structures and present a method that allows one to follow changes in the optical spectra of such systems as the concentrations of resident electrons and holes vary.

2. Excitons and trions in two-dimensional systems

As the dimension of a structure decreases, the efficiency of the Coulomb interaction between charge carriers increases significantly. For example, as already noted, the binding energy of a two-dimensional exciton increases by a factor of four compared to the bulk value. The increase in the binding energy of more sophisticated Coulomb complexes can be even

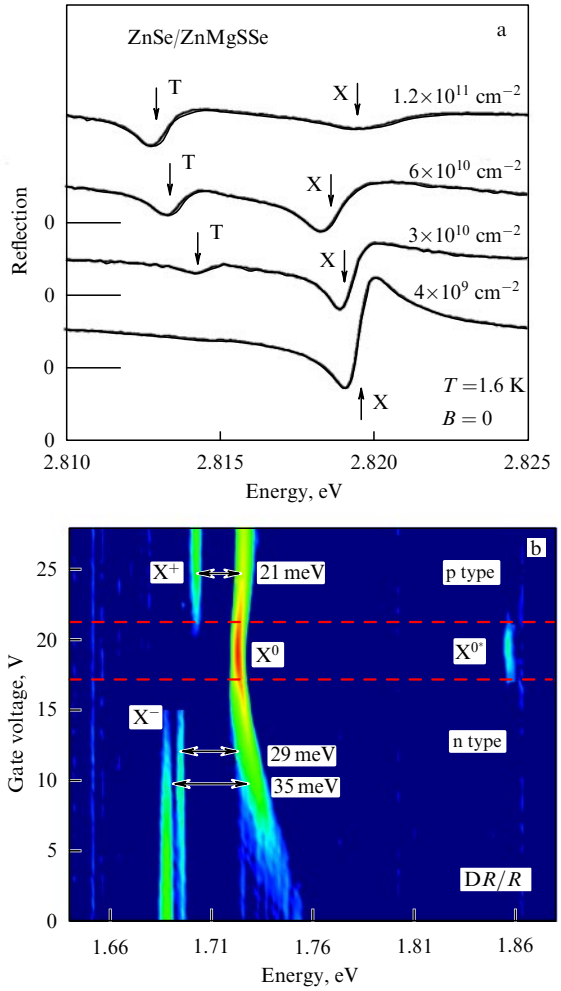

Figure 1. (a) Reflection spectrum of a ZnSe/ZnMgSSe quantum well near the exciton resonance at different concentrations of electrons [58]; (b) differential reflection spectrum of a van der Waals heterostructure with a WSe_2 monolayer, with a gated structure that allows changing the concentration of charge carriers [59].

greater. Excitons, and after the appearance of [22], also trions, are actively studied in two-dimensional structures such as quantum wells and, in the last two decades, in structures with extreme two-dimensionality: monatomic layers of transition-metal dichalcogenides. In Fig. 1, we show the reflection spectrum of a quantum well and the differential reflection spectrum of the van der Waals heterostructure with a WSe_2 monolayer near the exciton transition energy at various concentrations of charge carriers. In the neutral regime, only the resonance associated with the exciton can be seen in both graphs. In the presence of a sufficient concentration of free charge carriers, trions also begin to appear in the reflection spectra. At high concentrations, many-particle effects become significant, which is to be discussed separately. The respective exciton and trion binding energies in quantum-well structures typically reach several tens or a few meV. In structures with monolayers of transition-metal dichalcogenides, they are hundreds and tens of meV for excitons [47] and trions [60, 61]. In addition, the exciton series in monolayers of transition-metal dichalcogenides differs significantly from the hydrogen-like series [47]. As can be seen from Fig. 1, trions are observed at a nonzero concentration of resident charge carriers, and can therefore be described, starting from a certain concentration determined by the structure parameters, as Fermi polarons, i.e., excitons interacting with a degenerate electron (hole) gas (see Section 7).

2.1 Quantum-well structures

In quantum wells free of inhomogeneities, the motion of charge carriers is confined along one direction (chosen as the z-axis in what follows) and is free in the other two. In narrow quantum wells, in which the localization length of electrons and holes along the z-axis is much shorter than the characteristic size a_B of a bulk exciton (for example, about 120 Å in GaAs and about 30 Å in ZnSe), the size quantization energy of charge carriers is much greater than the binding energy of the bulk exciton. Compared to size quantization, the Coulomb interaction can then be considered a perturbation, and it is convenient to proceed from a three-dimensional problem to a two-dimensional one, separating the motion of charge carriers along the z-axis and in the plane of the structure. In this case, the electron–hole effective interaction potential has the form [62]

$$\widehat{V}_C(\boldsymbol{\rho}_e, \boldsymbol{\rho}_h) = -\int_{-\infty}^{\infty}\int_{-\infty}^{\infty} \frac{e^2}{\varepsilon\sqrt{(\boldsymbol{\rho}_e - \boldsymbol{\rho}_h)^2 + (z_e - z_h)^2}} \times \left|\Psi_e^0(z_e)\right|^2 \left|\Psi_h^0(z_h)\right|^2 dz_e\, dz_h\,, \quad (1)$$

where e is the electron charge, ε is the dielectric constant, $\Psi_e^0(z_e)$ and $\Psi_h^0(z_h)$ are the size quantization wave functions of the electron and the hole along the growth axis of the quantum well, and $\boldsymbol{\rho}_{e,h}$ and $z_{e,h}$ are the electron and hole coordinates in the quantum well plane and in the perpendicular direction. In narrow deep quantum wells, potential (1) can often be approximated by the two-dimensional Coulomb potential

$$\widehat{V}_C(\boldsymbol{\rho}_e, \boldsymbol{\rho}_h) = -\frac{e^2}{\varepsilon|\boldsymbol{\rho}_e - \boldsymbol{\rho}_h|}\,. \quad (2)$$

In the absence of inhomogeneities, the exciton center-of-mass motion is free, and the relative motion of the electron and the hole is described by a wave function that is a solution of the two-dimensional Schrödinger equation with effective potential (1) and the reduced exciton mass $1/\mu = 1/m_e + 1/m_h$. In the two-dimensional limit, the exciton problem reduces to the two-dimensional hydrogen atom problem, and the complex structure of the valence band can be neglected [62].

In a quantum well with an infinite barrier, the exciton binding energy would increase monotonically as the well width decreases. This is not the case with real quantum wells. In narrow quantum wells with a finite barrier, the exciton wave function penetrates the barrier, and its binding energy decreases and tends to the bulk value for the barrier material [63].

The problem of a two-dimensional trion is complicated by the fact that the masses of electrons and holes can be comparable, in contrast to three-particle complexes such as the H^- ion, the H_2^+ molecular ion, or a D^- center (two electrons localized on a charged impurity), where the mass of charge carriers of one type is much greater than that of another type. The development of computation technologies has allowed solving the problem of a three-particle Coulomb complex with very high accuracy using variational methods with a large (up to 10^4) number of parameters [64–66].

Another approach is to use variational methods with a small number of parameters endowed with a physical interpretation. This makes it possible to achieve greater clarity and obtain more general results at lower computational costs, even if at the cost of some loss of accuracy.

The binding energy of the H^- ion was first calculated by Bethe in 1929 [10]; he used a variational method with a function with three fitting parameters. The calculation was significantly refined by Chandrasekhar, who also used a function with three parameters, but in a form that was more suitable for the physical picture of the H^- ion structure (the normalization constants are omitted here and hereafter in this review) [67]:

$$\Psi_{H^-} = \left[\exp\left(-\alpha_1 r_1 - \alpha_2 r_2\right) + \exp\left(-\alpha_1 r_2 - \alpha_2 r_1\right)\right] \times \left(1 + c|\mathbf{r}_1 - \mathbf{r}_2|\right), \quad (3)$$

where $\alpha_{1,2}$ and c are fitting parameters and $r_{1,2}$ are the coordinates of electrons with respect to the nucleus. The factor $(1 + c|\mathbf{r}_1 - \mathbf{r}_2|)$, often called the polarization term, allows optimizing the contribution of repulsion between electrons.

The structure of the X^- trion is similar to that of the H^- ion in the entire range of the ratio σ of the electron and hole effective masses, and trial function (3) is well suited for its description, including in narrow quantum wells (when three-dimensional coordinates are replaced by two-dimensional ones). The picture is more complicated for the X^+ trion: its structure resembles that of the H_2^+ ion only for $\sigma \lesssim 0.1-0.2$, and for higher σ is somewhat closer to that of H^-. After the experimental discovery of trions, studies appeared devoted to the calculation of their binding energies based on the trial functions corresponding to (3) [13, 19, 21], which cannot describe the X^+ trion at low mass ratios even if 22 fitting parameters are used [21]. The correlated Gaussian method [68] and the model potential approximation [69] were used in addition.

In [70], a trial function was proposed that, on the one hand, can take the form of Chandrasekhar function (3) and, on the other hand, can describe the transition to the limit of the H_2^+ molecular ion:

$$\Psi_{tr} = \left[\exp\left(-\alpha_1 r_1 - \alpha_2 r_2\right) + \exp\left(-\alpha_1 r_2 - \alpha_2 r_1\right)\right] \times \frac{1 + cR}{1 + d(R - R_0)^2} \exp\left(-sR\right), \quad R = |\mathbf{r}_1 - \mathbf{r}_2|, \quad (4)$$

where $\alpha_{1,2}$, c, d, R_0, and s are fitting parameters with a clear physical meaning (see [70] for details). Trial function (4) allows describing both types of trions in the entire range of σ.

In Fig. 2, we show how the ratio of the binding energy of two-dimensional X^- and X^+ trions to the exciton energy depends on the ratio of the electron and hole effective masses (the hole is assumed to be heavier than the electron): (*1*) is the variational calculation with function (4) in [70], (*2*) is a calculation with 22 parameters in [21], and (*3*) is a calculation with the trion model potential in [69]. We note that the binding energies in Fig. 2 are given with the reversed sign. In [70], the relative error was estimated as $\lesssim 5\%$.

The H^- ion has no excited states [71], and the same is observed in two-dimensional systems, e.g., for D^- centers [72]. But the H_2^+ ion has many excited states, both with an excited electron in the field of nuclei that are in the ground state and with nuclei whose wave function is antisymmetric in its coordinate part. Hence, there is a critical value of the ratio

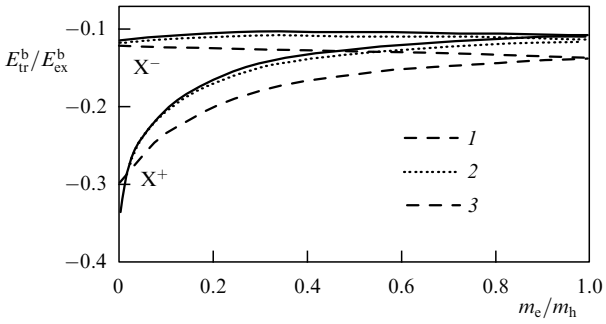

Figure 2. Dependence of the ratio of the binding energy of two-dimensional trions to the exciton energy on the effective mass ratio of the electron and hole. Curve *1* — [70], variational calculation with function (4); curve *2* — [21], calculation with 22 parameters; curve *3* — results in [69].

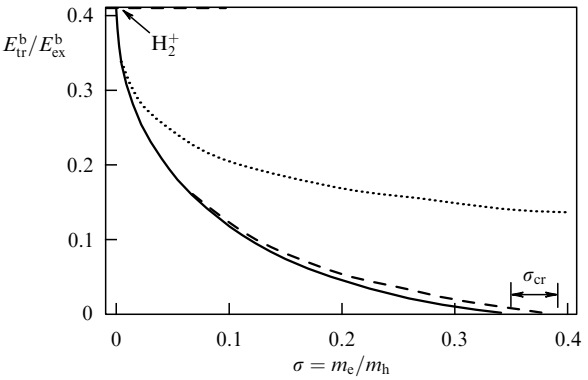

Figure 3. Dependence of the ratios of the binding energies of the triplet state of an X^+ trion to the exciton binding energy on σ, found variationally (solid curve) and adiabatically (dashed curve); dotted curve shows the binding energy of the ground state of the X^+ trion [73].

of electron and hole masses σ_{cr} at which the excited states disappear.

In [73], the σ dependence of the binding energy X^+ was studied for a trion with an antisymmetric coordinate wave function of two holes (such a state is often called a triplet state). In the variational method, the trial function

$$\Psi_{tr} = \left[\exp\left(-\alpha_1 r_1 - \alpha_2 r_2\right) + \exp\left(-\alpha_1 r_2 - \alpha_2 r_1\right)\right] \times \frac{\exp\left(-sR\right)}{1 + d(R - R_0)^2} R \exp\left(i\Theta_R\right), \quad R = |\mathbf{r}_1 - \mathbf{r}_2| \quad (5)$$

was used, where Θ_R is the angle between the vectors $\mathbf{r}_1$ and $\mathbf{r}_2$. The factor $R\exp(i\Theta_R)$ allows taking the antisymmetry into account and corresponds to the orbital angular momentum 1.

The solid curve in Fig. 3 shows how the ratio of the triplet-state binding energy of the X^+ trion to the binding energy of the exciton depends on the mass. The dependence was calculated by variation using function (5). The dotted curve shows the ground-state binding energy. As we can see, there is a critical value of the mass ratio at which the triplet bound state disappears, the upper bound for it being $\sigma_{cr} < 0.39$ [73].

2.2 Van der Waals heterostructures with monolayers of transition-metal dichalcogenides

Over the last two decades, the physics of nanostructures has been enriched with a new class of two-dimensional systems, two-dimensional crystals, including monomolecular layers of

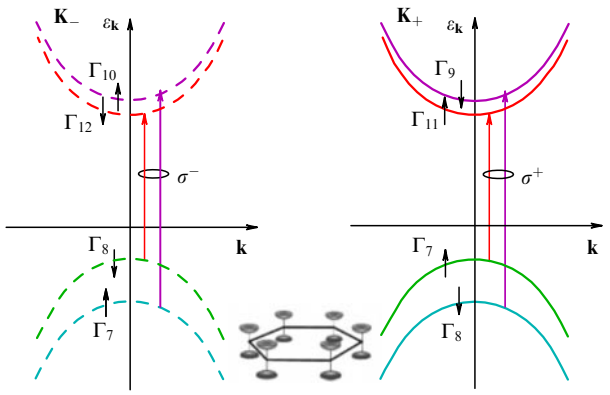

Figure 4. (Color online.) Schematic of energy dispersion near the **K** points of the Brillouin zone and selection rules for circular-polarization light incident on MoS_2 and $MoSe_2$ monolayers. The spin subbands of the conductance band in WS_2 and WSe_2 are ordered differently. Inset: a scheme of the Brillouin zone dispersion near the $\mathbf{K}_\pm$ points [49].

transition-metal dichalcogenides, which are described by the chemical formula MX_2 (where M is a transition metal, usually Mo or W, and X is a chalcogen, most commonly, S, Se, or Te). In contrast to graphene, where the valence and conduction bands join at the **K** and **K**′ points (sometimes denoted as $\mathbf{K}_\pm$) at the boundaries of the Brillouin zone, the presence of different atoms in the unit cell of MX_2 monolayers leads to a gap opening at these points [45, 46, 74]. The band structure of such monolayers is outlined in Fig. 4; they are direct-gap semiconductors with $E_g \approx 2$ eV [38–43]. Van der Waals heterostructures based on transition-metal dichalcogenides are being extensively studied [44].

As a result of a significant dielectric contrast between the monolayer material and the environment (a vacuum or air for a freely suspended monolayer or boron nitride in encapsulated structures), the interaction law of charge carriers is different from the Coulomb law [75–77]. The need to take the dielectric contrast into account when describing exciton effects in monolayer crystals was noted, e.g., in [47, 78, 79].

We consider a structure with two monolayers separated by a dielectric. The dielectric response of the layers is described by the two-dimensional polarizabilities $\varkappa_1$ and $\varkappa_2$ of the first and second layers; the permittivity of the environment ε is assumed to be constant. The difference between this approach and the classical one proposed in [75, 76] is that the layers are considered strictly two-dimensional. Solving a self-consistent problem yields the following Fourier transforms of the effective interaction potentials in a two-layer structure, where the two two-dimensional semiconductors with two-dimensional polarizabilities $\varkappa_1$ and $\varkappa_2$ are placed at a distance d from each other in a dielectric with permittivity ε [80, 81]: for charges located in the same layer,

$$\tilde{\varphi}_1 = \frac{2\pi e}{\varepsilon q} \frac{1 + qr_2(1-\xi^2)}{(1+qr_2)\left[1 + qr_1 - q^2 r_1 r_2 \xi^2/(1+qr_2)\right]}, \qquad (6)$$

and for charges located in two different layers,

$$\tilde{\varphi}_2 = -\frac{qr_1\tilde{\varphi}_1\xi}{1+qr_2} + \frac{2\pi e\xi}{\varepsilon q(1+qr_2)}. \qquad (7)$$

Here, $r_1 = 2\pi\varkappa_1$ and $r_2 = 2\pi\varkappa_2$ are the effective screening radii in the first and second layers, and $\xi = \exp(-q|z_1 - z_2|) = \exp(-qd)$ is a dimensionless parameter responsible for the efficiency of the electrostatic interaction of the layers. The electrons and holes are assumed to be located in different layers.

In the limit of a long interlayer distance $d \to \infty$, we have $\xi \to 0$, and the effect of the second layer can be neglected. Expression (6) then becomes

$$\tilde{\varphi}_1 = \frac{2\pi e}{\varepsilon q(1+qr_1)}. \qquad (8)$$

In coordinate form, this can be written as [75, 76, 78, 82, 83]

$$\varphi(r) = \frac{\pi e}{2\varepsilon r_1}\left[\mathrm{H}_0\left(\frac{r}{r_1}\right) - \mathrm{Y}_0\left(\frac{r}{r_1}\right)\right], \qquad (9a)$$

where H_0 and Y_0 are the Struve and Neumann functions. In a number of studies, the new screening radius $\tilde{r}_1 = \varepsilon r_1$ is used instead of r_1, which allows writing the potential as

$$\varphi(r) = \frac{\pi e}{2\tilde{r}_1}\left[\mathrm{H}_0\left(\frac{\varepsilon r}{\tilde{r}_1}\right) - \mathrm{Y}_0\left(\frac{\varepsilon r}{\tilde{r}_1}\right)\right]. \qquad (9b)$$

Expressions (9) are referred to in the literature as the Rytova–Keldysh potential. A similar problem for superlattices was solved in [84]. Screening due to free charge carriers turns out to be insignificant when calculating the binding energies of electron–hole complexes in MX_2 (see, e.g., [85]).

In monolayers of transition-metal dichalcogenides, two types of excitons are observed: the A exciton, formed by the states of the upper valence band and the lower conduction band (the corresponding transitions are shown by red arrows in Fig. 4), and the B exciton, in which the electron and hole are in spin–orbit decoupled bands. In Fig. 5, we show the results of measurements of the reflection spectrum of a van der Waals structure with an MoS_2 monolayer in the exciton resonance region [86]. The sample scheme is shown in Fig. 5a, b. The measured spectrum (black dots in Fig. 5c) exhibits three peaks associated with the A exciton and one broader peak corresponding to the ground state of the B exciton.

Near the band extrema, the dispersion of both electrons and holes in monolayers of transition-metal dichalcogenides can be described with good accuracy as a simple one, which greatly simplifies the calculations. The exciton binding energy can be easily calculated by directly solving the Schrödinger equation, which is, in fact, one-dimensional. Because the effective electron–hole interaction potential is different from the Coulomb one, it is justifiable in the variational calculation to use a more complex trial function than the hydrogen-like one,

$$\varphi_{\mathrm{ex}}(\rho) \propto \exp(-\alpha\rho) + \delta\rho\exp(-\beta\rho), \qquad (10)$$

with three fitting parameters: α, δ, and β. This allows taking the admixture of the first excited complex to the ground state of a hydrogen-like complex into account. Here, ρ is the modulus of the radius vector of the relative position of the electron and hole $\boldsymbol{\rho}$. A comparison with numerical calculations showed that function (10) provides an error of no more than 1% in calculating the exciton energy. Fitting one parameter, the effective screening radius, whose value is in reasonable agreement with atomistic calculations [78], allows reliably reproducing the positions of the A exciton in the spectrum in Fig. 5. This indicates the applicability of the

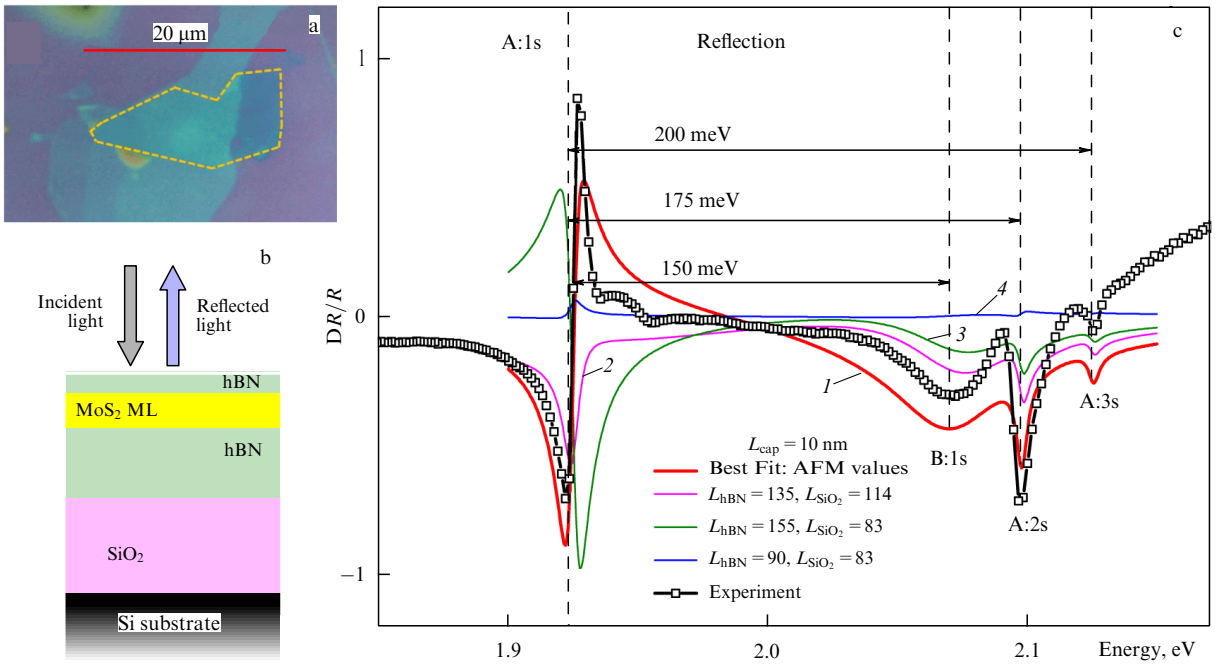

Figure 5. (Color online.) (a) Optical microscope image of an MoS_2 layer encapsulated in hexagonal boron nitride (hBN). (b) Scheme of the structure: upper (lower) hBN layer has a thickness of 7 ± 3 nm (130 ± 5 nm) according to atomic-force microscopy (AFM) data, and SiO_2 layer has a thickness of 83 nm. (c) Differential reflection spectrum DR/R. Bold red line *1*: calculation using hBN thicknesses determined by AFM. Additional calculations (purple (*2*), green (*3*), and blue (*4*) lines) for different hBN and SiO_2 thicknesses (see inset) show how the depth and shape of exciton resonances depend on the thickness of individual layers [86].

Rytova–Keldysh potential to describing the interaction of charge carriers in monolayers of transition-metal dichalcogenides.

An interesting feature of the reflection spectrum in Fig. 5c shows a significant optical response of the 2s and 3s excited states of the A exciton, exceeding the estimates for the exciton where the electron and hole are assumed to interact via the Rytova–Keldysh potential. Such a difference between the simplest theory and experiment indicates the need to take the multiple reflection of light into account in the van der Waals heterostructure (Fig. 5b), which leads to the appearance of the Purcell effect [87].

Compared with classic two-dimensional semiconducting structures (quantum wells), trions in monolayers of transition-metal dichalcogenides have specific features. First, trions are observed at up to room temperatures, which is due to their significant binding energy [88–90]. Second, the existence of two valleys **K** and **K′** in the band structure of MX_2 monolayers, as well as the spin splitting of the conduction band, determine the presence of several different spin and valley configurations for charge carriers [91].

In Fig. 6, we show the main experimental data from [59]. A sample under study had a WSe_2 monolayer encapsulated in hexagonal boron nitride, placed in a structure with electrodes (see the diagram in Fig. 6a); applying a voltage to the electrodes allows controlling the concentration and type of resident charge carriers in the monolayer. Figure 6c shows the differential reflection spectrum DR/R. In the p-doping regime, when the Fermi level is in the valence band, a positively charged trion (X^+) is observed at an energy 21 meV below the exciton line. In the neutral regime, when the Fermi level is between the valence and conduction bands, only an exciton (X^0) with the transition energy of 1.72 eV and its excited state (X^{0*}) are observed. In the n-doping regime, when the Fermi level is in the conduction band, the X^- trion can be seen in the spectrum, and its line is a doublet split by 6 meV: two transitions are observed 29 and 35 meV below the X^0 exciton line. This splitting is due to the fine structure of the trion (see below). Trions are also observed in photoluminescence spectra (Figs 6d–f). In the nonencapsulated sample (Fig. 6b), the emission lines are noticeably wider, but the line corresponding to the X^- trion is also visible. Van der Waals gated structures are currently being extensively studied (see [92] and the references therein). Not only excitons and trions but also more intricate complexes are observed.

For a theoretical description, due to a significant ($\gtrsim 100$ meV) spin–orbit splitting of the valence band, it suffices to take the ground spin state of a hole into account in a specific valley [93]. Holes are described by one valley index. For an electron, it is necessary in general to take both spin states into account, because the splitting of the conduction band is smaller, given by tens of meV. Hence, there are two indices for electrons: spin and valley. According to the general rules of quantum statistics, the total trion wave function must be antisymmetrized with respect to permutations of identical charge carriers. The envelope function of the relative motion must be symmetric under permutations of identical charge carriers if the two-particle Bloch function is antisymmetric, and vice versa. Such trions are called *symmetric* or *antisymmetric* according to the permutation symmetry of the envelope function. For symmetric trions, two identical charge carriers cannot be in the same band: their spin and/or valley indices must be different. In heterostructures based on III–V and II–VI semiconductors, in which there are no valley degrees of freedom, the term ‘singlet’ trion is used for the symmetric state and ‘triplet’ trion for the

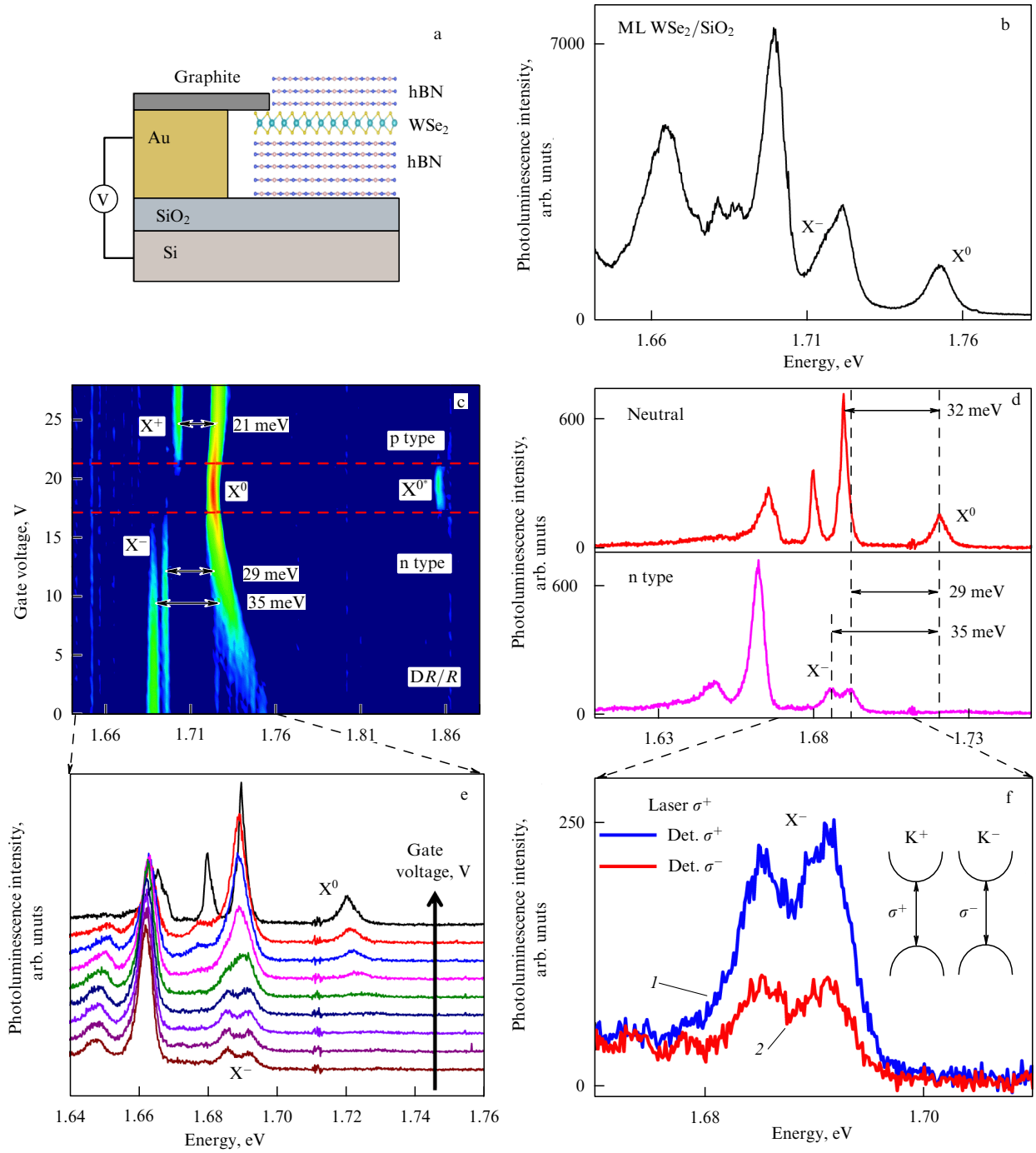

Figure 6. (Color online.) (a) Schematic of a van der Waals heterostructure with controlled charge state of the WSe_2 monolayer. (b) Typical photoluminescence spectrum of a WSe_2 monolayer on SiO_2 without encapsulation. Shown are the (X^-) trion peak and the neutral exciton (X^0) peak. (c) Differential reflection DR/R of a WSe_2 sample encapsulated in hexagonal boron nitride (Fig. a). Shown are ranges of gate voltage corresponding to n and p doping. (d) Photoluminescence spectra in neutral regime (above) and in the presence of resident electrons (below). (e) Evolution of photoluminescence upon changing the doping regime from neutral to the n type. (f) Photoluminescence of an X^- trion under excitation by σ^+ light in two polarizations of detection (σ^+ — blue curve *1*; σ^- — red curve *2*) [59].

antisymmetric state, referring to the corresponding spin configuration of a pair of electrons or holes.

The variational approach is often used to calculate trions in MX_2 monolayers. In addition to the stochastic variational method [94] introduced in [68], an approach that is also in use involves simpler trial functions with a small number of parameters endowed with a clear physical meaning. For example, in [78], a simple two-parameter trial function was used, given by the Chandrasekhar function without a polarization term, and the interaction of charge carriers was described by the Rytova–Keldysh potential. This greatly simplifies the calculations and makes it easy to obtain reasonable estimates for the binding energy of trions, but the possibility is lost of determining the dependence of the binding energy of trions on the ratio of electron and hole masses. It can be determined using a slightly more complex function (4) used in [59]. Function (5) was used to calculate the binding energy of antisymmetric trions.

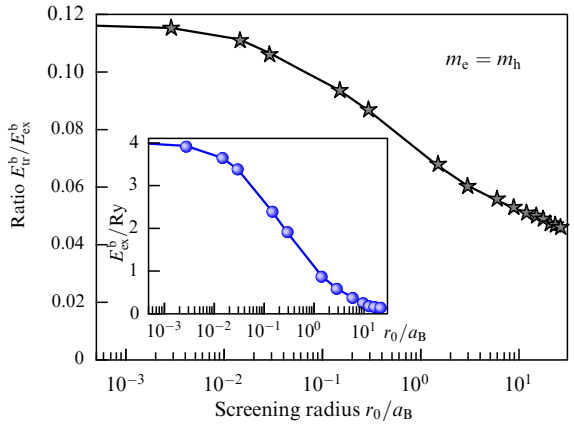

Figure 7. Ratio of trion binding energy E_{tr}^b to exciton binding energy E_{ex}^b as a function of screening radius r_0 at equal electron and hole masses. Inset shows the exciton binding energy as a function of r_0 [59].

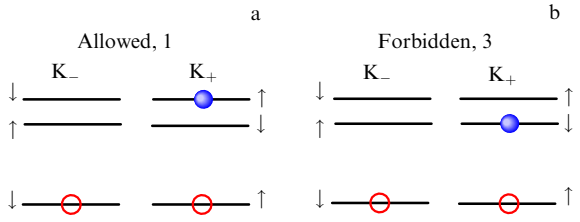

Figure 8. Schematic illustration of the symmetric X^+ trion: (a) state 1 and (b) state 3. Blue dots show electrons in the conductance band, and circles show unfilled states in the valence band. Order of conductance subbands corresponds to WSe_2 [59].

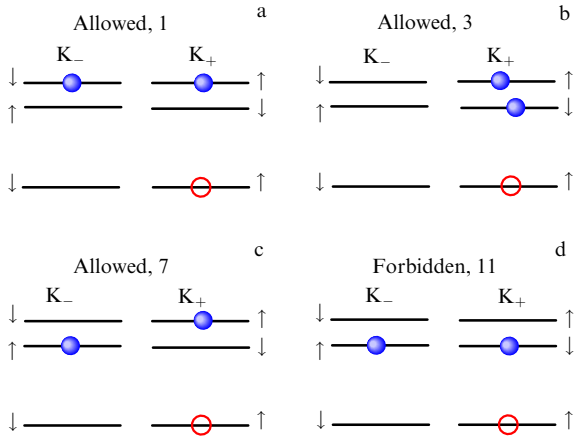

Figure 9. Examples of symmetric X^- trions: (a–c) optically active states, (d) dark state. Order of conductance subbands corresponds to WSe_2 [59].

The ratio of the binding energies of the trion E_{tr}^b and the exciton E_{ex}^b calculated with trial function (4) depending on the screening parameter r_0 for equal effective masses of electrons and holes (the effective masses being in fact sufficiently close in magnitude) is shown in Fig. 7. The inset shows the exciton binding energy E_{ex}^b. Dimensionless units corresponding to bulk Bohr units with the reduced mass μ and dielectric constant ε are used in Fig. 7. The screening radius $r_0 = 0$ corresponds to the two-dimensional Coulomb problem. As r_0 increases, the interaction potential becomes shallower, and the exciton and trion binding energies and their ratio E_{tr}^b/E_{ex}^b decrease. A comparison of the results of calculations of the trion binding energies with those using the quantum Monte Carlo method in [95] shows a good calculation accuracy (typical error is less than 5%). The binding energies of trions of both types turn out to be not very sensitive to the ratio of effective masses m_e/m_h in the range corresponding to the experiment ($\sigma \sim 1$).

At $m_e = 0.28m_0$, $m_h = 0.36m_0$ [74], $\varepsilon = 1$, and $r_0 = 40$ Å, the neutral exciton binding energy E_{ex}^b turns out to be 500 meV, which agrees with experiments [47, 96, 97], and the binding energies of the X^+ and X^- trions are $E_{X^-}^b \approx E_{X^+}^b = (26 \pm 1)$ meV. This value is in reasonable agreement with the experimental data presented in Fig. 6c: somewhat higher than the measured binding energy of the X^+ trion (21 meV) and somewhat lower than the 'average' (over the center-of-mass position of the doublet) binding energy of the X^- trion (32 meV). Experimental data can also be reasonably described for $\varepsilon \neq 1$; for example, at $\varepsilon = 3.3$, $\mu = 0.16m_0$, and $r_0 = 6.4$ Å, the energies $E_{ex}^b = 283$ meV and $E_{tr}^b = 20.6$ meV can be obtained. Experiment shows that the binding energy of the X^+ trion is less than the binding energy of the X^- trion, but the point of view prevails in the literature that $m_e \lesssim m_h$ in MX_2 [74]. For such a mass ratio, the ratio between the binding energies of trions should be the inverse. But, even if we assume that $m_e > m_h$ in WSe_2, the effective mass ratio σ for an electron and a hole should be unrealistically large, given the 10 meV difference between the binding energies of the X^+ and X^- trions: $m_h/m_e > 10$. New data on magnetotransport [98, 99] and an analysis of the role of polaron effects in MX_2 monolayers [100] suggest that $m_e/m_h \lesssim 2$. However, this is still not enough to explain the difference between the X^- and X^+ binding energies observed in experiments [59, 92]. In addition, the considered model does not allow describing the splitting of the X^- trion line in structures with tungsten-based monolayers [59, 92, 101].

The fine structure of the states of the *symmetric* X^+ trion is quite simple: two holes form a spin and valley singlet, and the electron is in one of the four possible states of the conduction band (see [59] for a detailed derivation). Of the four states of the X^+ trion, two are dark and two are optically active in circular polarizations $\sigma^\pm$ for radiation normally incident on the monolayer. Examples of the light and dark states of the X^+ trion are shown in Fig. 8. For a given polarization, there is therefore only one optically active state of an X^+ trion, in agreement with the experimental data in Fig. 6c.

The situation is more intricate for negatively charged trions, because the electron can occupy both the lower and upper spin subbands of the conduction band. Analyses show that there are 12 states of the X^- trion, which differ in spin/valley configurations of charge carriers, three of which are optically active Kramers-degenerate pairs. However, the allowed X^--trion states 1 and 2 (Fig. 9) contain electrons from the upper conduction subbands. The splitting of the conduction band for a WSe_2 monolayer is equal to about 40 meV [102]. As a result, at experimentally attainable electron concentrations $n_e \lesssim 4 \times 10^{12}$ cm^{-2} and at cryogenic temperatures, the population of the excited subbands is negligible. The trion state 1 and the corresponding Kramers-degenerate state cannot form in the process of single-photon absorption and are therefore not active in absorption/reflection. Thus, under the experimental conditions, only two pairs of states, 3 (together with the corresponding

Kramers-degenerate state) and 7 (together with the corresponding Kramers-degenerate state) (Fig. 9b, c), are responsible for the two observed reflection lines (Fig. 6c).

These pairs of X^- trion states have the same energy in the framework of the effective mass method. The splitting between them, as well as the difference between the binding energies of X^+ and X^- trions, may be due to short-range contributions to the electron–electron exchange interaction [103]. Estimates show that, for realistic parameters, it is possible to obtain a ~ 6 meV difference between the binding energies of trions, which agrees with the experimentally observed splitting of the X^- trion lines [59]. The contributions to the fine structure of trions from electron–hole exchange are also similar by order of magnitude. Short-range contributions can also lead to differences between the energies of X^+ and X^- trions. For MoX_2 monolayers, with opposite-sign spin splitting of the conduction band, no fine structure of the X^- trion is expected.

3. Excitons and trions in quasi-one-dimensional systems

Excitons and trions are also observed in semiconducting quantum wires [29, 104], structures in which the motion of charge carriers is confined to two directions and is free along the third dimension. The binding energy of an X^- trion in a GaAs-based quantum wire, determined experimentally in [29], is 2.3 meV, which is much higher than the values of 0.9–1.2 meV for GaAs quantum wells [105–107].

The theoretical description of electron–hole complexes in quantum wires is known to have no one-dimensional limit. The binding energy of complexes experiencing Coulomb interaction diverges logarithmically as the wire radius tends to zero [108]. As a result, in the quantum wire structures of finite radius studied in experiments, the binding energies of Coulomb complexes increase significantly compared to bulk semiconductors [24–27, 104]. From the theoretical standpoint, the divergence prevents one from taking a zero-radius quantum wire as a starting point, unlike the case with a zero-width quantum well. A similar situation occurs in the description of excitons and trions in bulk semiconductors in a strong magnetic field, because the motion of carriers is quantized in the plane perpendicular to the field, while being free along the field [108].

3.1 Binding energy of an exciton in a quantum wire

In this section, we use volumetric units for energy and length: the exciton Rydberg radius and the Bohr radius. If the localization radius of charge carriers within the cross section of a quantum wire is much smaller than the Bohr radius, then the coordinates of the transverse motion of the electron and the hole can be separated.

After averaging the exciton Hamiltonian over the variables $\boldsymbol{\rho}_e$ and $\boldsymbol{\rho}_h$, we obtain the effective one-dimensional electron–hole interaction potential

$$\widehat{V}_C(z) = -\int_0^\infty \int_0^\infty \frac{2}{\sqrt{(\boldsymbol{\rho}_e - \boldsymbol{\rho}_h)^2 + z^2}} \times \left|\Psi_e^0(\boldsymbol{\rho}_e)\right|^2 \left|\Psi_h^0(\boldsymbol{\rho}_h)\right|^2 d\boldsymbol{\rho}_e\, d\boldsymbol{\rho}_h\,, \tag{11}$$

where $z = z_e - z_h$, and $\Psi_e^0(\boldsymbol{\rho}_e)$ and $\Psi_h^0(\boldsymbol{\rho}_h)$ are the wave functions of the ground state of the transverse motion of an isolated electron and a hole. We note that the factor 2 in the numerator in (11) appears due to switching to dimensionless variables. For the effective electron–hole interaction potential, the approximation [109–115]

$$\widehat{V}_{\text{eff}}(z, a) = -\frac{2}{\sqrt{z^2 + a^2}} \tag{12}$$

is widely used, where the parameter a plays the role of the effective radius of the quantum wire.

The Coulomb repulsion between charge carriers of the same sign is described by an effective potential similar to (11). Because the wave functions of the transverse motion of an electron and a hole can be different in the general case, the resulting effective radius of the wire is different from that in (12). But this effect is usually neglected, and the repulsion between likely charged carriers is assumed to be described by the potential $\widehat{V}'_{\text{eff}}(z, a) = -\widehat{V}_{\text{eff}}(z, a)$, which differs from the electron–hole attraction potential only by sign.

To find the binding energy of an exciton within the variational method, it is reasonable to use the simplest trial function [116]

$$\varphi_\alpha(z) = \exp\left(-\alpha|z|\right) \tag{13}$$

with a single fitting parameter α. The binding energy of an exciton in a quantum wire depends on its radius logarithmically. It is therefore convenient to introduce the parameter $\gamma = \ln(a_B/a)$. For $\gamma \gg 1$, the binding energy has the asymptotic form [108]

$$E_{ex}^b = 4\gamma^2 = 4\ln^2\left(\frac{a_B}{a}\right). \tag{14}$$

The ratio between the size of the cross section of the quantum wire and the parameter a can be reasonably chosen such that the exciton binding energies calculated by direct diagonalization of the Hamiltonian with potentials (11) and (12) coincide. Approximation (12) then gives good agreement with the exact calculation in the entire range of γ, including the region $\gamma \gtrsim 1$ corresponding to real semiconducting quantum-wire systems. For $\gamma \gg 1$, the result of the variational calculation tends to be exact, but even in the region $\gamma \sim 1$, where function (13) is the least accurate, the relative error in calculating the binding energy is no more than 6% [116].

Interestingly, asymptotic form (14) is realized only for nonphysical values of the parameter γ ($\gamma > 50$) due to the slow decrease in the following correction to (14):

$$E_1 \approx -8\gamma\,(\ln 2\gamma + 1{,}3)\,. \tag{15}$$

Estimates show that, for example, for the parameters of GaAs, the quantum wire radius becomes comparable to the interatomic distance already at $\gamma = 4$.

3.2 Trions in quantum wires

There are a number of experimental and theoretical [117–119] studies of trions in quasi-one-dimensional systems. Numerical diagonalization of the Hamiltonian is used to find the binding energy of trions in quantum wires [26, 118–120]. In [117], using the variational method, the limit case of very small radius quantum wires was studied; wires with realistic radii were considered in [116].

In [116], trial functions constructed similarly to the quantum-well functions for [121] were used to find the

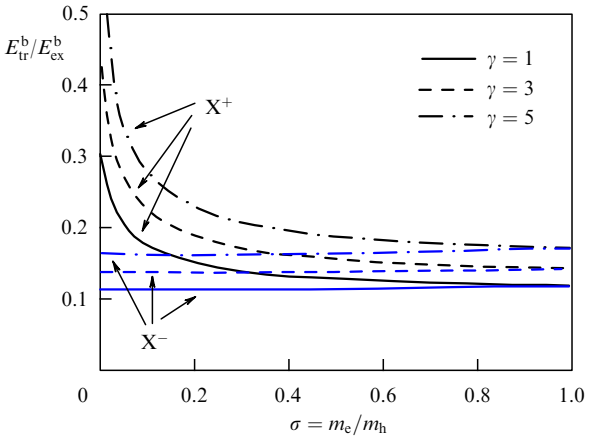

Figure 10. Dependence of the ratio of the singlet-state binding energy of X^+ and X^- trions to the exciton binding energy on ratio σ of effective electron and hole masses, evaluated for several values of parameter $\gamma = \ln(a_B/a)$. Trial function (16) was used [116].

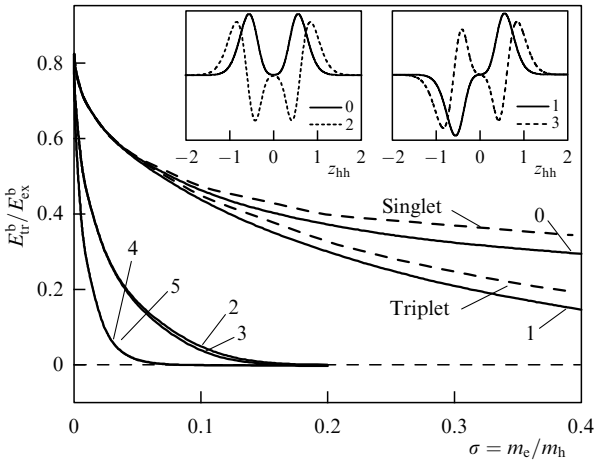

Figure 11. Dependence of the binding energy of the first six states in potential V_{ad}^0 on electron and hole mass ratio σ for $\gamma = 1$. Dashed lines show numerically obtained dependences for singlet and triplet states of the X^+ trion. Insets show non-normalizable wave functions of the four lower states [116].

binding energies of X^- and X^+ trions: the function

$$\Psi^s(z_1, z_2) = \left[\exp\left(-\alpha|z_1| - \beta|z_2|\right) + \exp\left(-\alpha|z_2| - \beta|z_1|\right)\right] \times \exp\left(-\delta\left||z_1 - z_2| - R_0\right|\right) \quad (16)$$

for the singlet state of trions, i.e., states of a pair of identical particles with zero total spin and with the spatial function symmetric under permutations of identical charge carriers, and the function

$$\Psi^t(z_1, z_2) = (z_1 - z_2)\left[\exp\left(-\alpha|z_1| - \beta|z_2|\right) + \exp\left(-\alpha|z_2| - \beta|z_1|\right)\right] \exp\left(-\delta\left||z_1 - z_2| - R_0\right|\right) \quad (17)$$

for the triplet state. Function (16) is a modified trial function for a two-dimensional trion proposed in [70].

In Fig. 10, we show the dependence of the ratio of the singlet-state binding energies E_{tr}^b of the X^+ and X^- trions to the exciton binding energy E_{ex}^b on the effective electron and hole mass ratio $\sigma = m_e/m_h$, calculated by the variational method in [116] for several values of the parameter γ associated with the radius of the quantum wire, using trial function (16). The binding energies of both types of trions increase as the effective radius of the quantum wire decreases, which is associated with an increase in the efficiency of the Coulomb interaction. The results presented in Fig. 10 were obtained for the same effective radii of the quantum wire for the electron and the hole. If the effective radii are different, then one of the types of trions may even turn out to be energetically disadvantageous in comparison with the exciton.

The dependences in Fig. 10 qualitatively reproduce the corresponding dependences for quantum wells. In a quantum well, however, the X^- trion binding energy varies more strongly as σ varies. The X^+ trion binding energy in a quantum well, on the contrary, varies less than in a quantum wire [116]. The triplet state of the X^+ trion turns out to be bound for any value of the mass ratio, and the triplet state of the X^- trion exists for $0.95 \lesssim \sigma \leqslant 1$. This is qualitatively different from the two-dimensional system, in which the X^- trion triplet state is not bound at all and the X^+ trion state is bound for $\sigma < \sigma_{cr} \approx 0.39$ [73]. A comparison with numerical calculations gave an estimate of the error in calculating the binding energy as no more than 10% of a singlet trion and no more than 2% for a triplet one.

The ground state of holes in the adiabatic potential $V_{ad}^0(z_{hh}, a)$ corresponding to the ground state of an electron in a field of immobile holes is the singlet state of the X^+ trion considered above, and the first excited state is the triplet state. Figure 11 shows the dependences of the binding energy of the first six states in the potential V_{ad}^0 on σ calculated for $\gamma = 1$. Dashed lines correspond to the binding energies of the singlet and triplet states calculated numerically. In the vicinity of $\sigma = 0$, the binding energies increase as $\sqrt{\sigma}$ as the mass ratio decreases, and the pairs of levels with numbers $2k$ and $2k + 1$ come closer to each other. Analyses show that for $\sigma < 0.2$ the error of the adiabatic approximation is no more than 10%. Localized states, albeit with much lower binding energies, also appear in the potential V_{ad}^1 that describes the first excited state of an electron in the potential produced by the holes. The trion states in this potential are similar to the antibonding states of molecular ions [116].

4. Excitons and trions in quasi-two-dimensional structures with spatial charge separation

In nanostructures with spatial charge separation, on the one hand, the binding energy of Coulomb complexes decreases, but, on the other hand, their lifetime increases. In addition, another parameter appears in the system, the distance between the regions in which the electrons and holes are localized, which makes it possible to control the properties of Coulomb complexes. An important property of spatially indirect excitons is their Bose–Einstein condensation [122–125].

4.1 Structures with double quantum wells

An example of structures in which spatial charge separation can be realized is given by double quantum wells [126–133]. Changing the distance between the wells allows significantly changing the shape of the effective electron–hole interaction potential. The effective electron–hole interaction potential can be represented as $V(\rho) \propto (\rho^2 + d^2)^{-1/2}$, where ρ is the

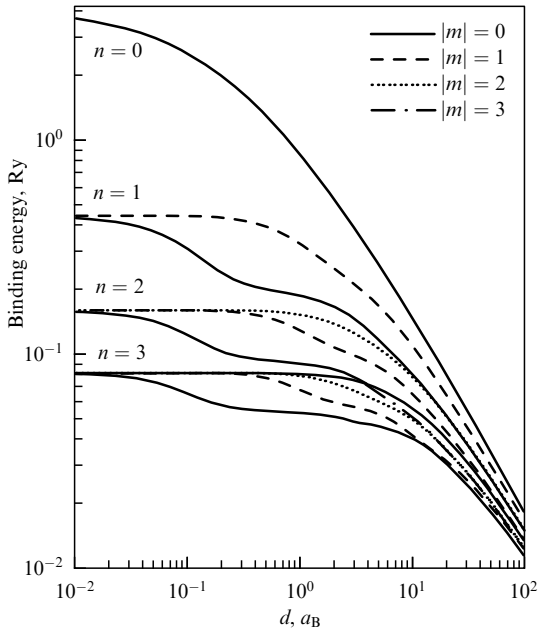

Figure 12. Dependence of the exciton binding energy on distance d between layers. Shown are dependences corresponding to first four levels in the limit case $d \to 0$ [133]. Binding energy and interlayer distance are expressed in terms of bulk exciton Bohr units.

relative coordinate of the electron and the hole in the plane of the structure and d is the distance between the quantum wells. Another suitable system is an electron in a δ-doped structure with a narrow quantum well that interacts with a donor located inside the barrier [134, 135]. In the limit $d \to 0$, the interaction potential tends to the Coulomb one, and for $d \to \infty$ it tends to the harmonic one.

A distinctive property of the Coulomb and harmonic potentials (both three- and two-dimensional) is the 'accidental' degeneracy of the energy levels, i.e., multiple additional degeneracy due to the presence of an additional nontrivial operator commuting with the Hamiltonian (in classical mechanics, an integral of motion) [136–140]. The degeneracy multiplicities of energy levels for the Coulomb and harmonic potentials are different, being respectively equal to $2n + 1$ and $n + 1$ in the two-dimensional case (where $n = 0, 1, 2, \ldots$ is the level number). In [133], the states of a spatially indirect exciton were calculated using numerical diagonalization of the matrix of the indirect exciton Hamiltonian (Fig. 12). Because the degeneracy multiplicities are different in the limit cases, the energy levels are rearranged in the transition region. As d increases, energy level splitting decreases, and the energy structure of a two-dimensional oscillator is restored.

At a long distance between the quantum wells, the binding energy of the ground state of a spatially indirect exciton decreases $\propto d^{-1}$. Theoretically, the exciton therefore exists at any d. This is not the case for trions; at sufficiently large d, the attraction between charge carriers of different types located in different quantum wells cannot balance the repulsion between charge carriers of the same type located in the same well, and the bound state of the trion disappears. In [132], the limit case of an X^+ trion with infinitely heavy holes in a structure with spatial charge separation was studied.

In Fig. 13, we show the calculated dependences of the binding energies of an exciton and an X^+ trion with infinitely heavy holes on the distance d between quantum wells. It can

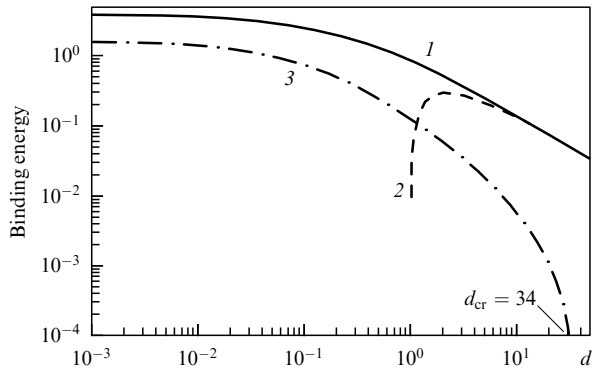

Figure 13. Dependence of exciton (*1*) and trion (*3*) binding energies on distance d between quantum wells; *2*—exciton binding energy approximation in the form $2/d - 2/d^{3/2}$. Energy and distance are measured in bulk exciton Bohr units [132].

be seen that there is a limit value $d_{cr} \approx 34a_B$ at which the bound state of the trion disappears. The value $d_{cr} \approx 34a_B$ is unrealistically large from the experimental standpoint for most semiconductors with $a_B = 20-150$ Å. For realistic values $d \approx a_B$, estimates in [132] give a trion binding energy of ~ 0.5 meV.

4.2 Heterostructures with monolayers of transition-metal dichalcogenides

The possibility of creating and actively studying van der Waals heterostructures and structures with several layers of transition-metal dichalcogenides (see, e.g., [141–146]) raises the acute problem of calculating Coulomb complexes in two-layer heterostructures based on transition-metal dichalcogenides with spatial separation of charge. For two-layer systems in which two monolayers are separated by a tunnel-impenetrable barrier, the question of the exciton–trion binding energy has been studied theoretically; in [147, 148], the screening of the Coulomb interaction was not taken into account, and in [149–151], self-consistent screening by two layers was ignored.[1] In [81], the potential

$$V_{eh}(\rho) = -\frac{1}{\pi}\int_0^\infty \mathrm{d}q\, \tilde{\varphi}_2 J_0(q\rho)\,, \tag{18}$$

where $\tilde{\varphi}_2$ is given in (7), was used as a two-dimensional effective electron–hole interaction potential in van der Waals heterostructures with spatial charge separation.

As $d \to 0$, potential (18) transforms into the Rytova–Keldysh potential, which, in contrast to the Coulomb one, does not have an extra symmetry leading to 'accidental' degeneracy. In the opposite limit, $d \to \infty$ (and $\rho > r_{1,2}$), the interaction potential, similarly to the case without dielectric contrast, can be approximated by the harmonic oscillator potential [151]. To calculate the ground-state energy, we use the variational method with the trial function

$$\Psi_{ex}(\rho, \alpha_1, \alpha_2, \beta, \delta) = \exp\left(-\alpha_1\rho - \beta\rho^2\right) + \delta\rho\exp\left(-\alpha_2\rho\right), \tag{19}$$

[1] In [149–151], the Rytova–Keldysh potential is used with the argument $\sqrt{\rho^2 + d^2}$. This approach does not take the self-consistent screening in a two-layer system into account. In the limit $d \to \infty$, the potential is also asymptotically parabolic.

where α_1, α_2, β, and δ are fitting parameters. The choice of a rather complex function is justified by the following circumstances: (1) as $d \to 0$, the potential $V_{eh}(\rho)$ differs significantly from the Coulomb one near the origin, and the second term with $\delta \neq 0$ allows taking the corresponding deviation from the hydrogen-like model into account; (2) for large d, the potential $V_{eh}(\rho)$ is well approximated by a harmonic potential. Thus, the introduction of a Gaussian factor in trial function (19) is justified. A comparison with numerical calculations allows estimating the error in calculating the exciton binding energy with trial function (19) as $< 1\%$ [81]. Calculations show that, at an interlayer distance of several nanometers, the binding energy of a spatially indirect exciton can be ~ 100 meV. In [81], a calculation is also given in the case $r_1 \neq r_2$.

In [81], a spatially indirect trion was considered, with two similarly-named charged carriers in one layer and the third in the other layer. The electron–hole interaction is given by (18), and the interaction of identical carriers is described by a similar expression with $\tilde{\varphi}_2$ replaced with $\tilde{\varphi}_1$ in (6) and with the sign reversed:

$$V_{ee}(\rho) = \frac{1}{\pi}\int_0^\infty \mathrm{d}q\, \tilde{\varphi}_1 J_0(q\rho)\,. \tag{20}$$

The closeness of the effective masses of charge carriers in transition-metal dichalcogenides allows simplifying the form of the trial function for trions. In particular, there is no need to use the wave function in a universal form applicable to the entire range of the electron and hole mass ratio for both types of trions, and it suffices to restrict ourselves to a function with 9 fitting parameters:

$$\begin{aligned}\Psi_{tr} = {} & \left[\Psi_{ex}(\rho_1,\alpha_1,\alpha_2,\beta_1,\delta_1)\Psi_{ex}(\rho_2,\alpha_3,\alpha_4,\beta_2,\delta_2)\right.\\ & \left.+\,\Psi_{ex}(\rho_2,\alpha_1,\alpha_2,\beta_1,\delta_1)\Psi_{ex}(\rho_1,\alpha_3,\alpha_4,\beta_2,\delta_2)\right]\\ & \times\left(1+c|\boldsymbol{\rho}_1-\boldsymbol{\rho}_2|\right),\end{aligned} \tag{21}$$

where Ψ_{ex} is defined in (19) and α_1, α_2, α_3, α_4, β_1, β_2, δ_1, δ_2, and c are fitting parameters.

The results of the calculation of the trion binding energy [81] are shown in Fig. 14. As for the exciton, two situations are considered: (1) both layers have the same effective screening radius $r_1 = r_2 = 1.65$ nm, and (2) the electrons are in the layer with $r_1 = 3.3$ nm and the hole is in the layer with $r_2 = 0$. In the case $r_1 = 0$ and $r_2 \neq 0$, i.e., when the electrons are in the layer without screening, the trion binding energy vanishes at finite values of r_2 due to the Coulomb repulsion between electrons, which is then strong compared with the attraction to holes. We can see from Fig. 14 that the trion binding energy, like the exciton binding energy, rapidly decreases as d increases. The trion binding energy in case 1 turns out to be higher than in case 2 due to the stronger Coulomb interaction, as in the case of the exciton binding energy. An essential point is that, even at large (~ 10 nm) distances between layers, the trion binding energy is equal to several meV and can be reliably measured in experiment. As in double quantum wells, the trion binding energy vanishes at the critical interlayer distance $d \sim 30a_B$ [132].

5. Electron–hole complexes localized in nanostructures at interface roughness

A comparison of theoretical calculations [152, 153] and experimental data for trion binding energies (quantum wells

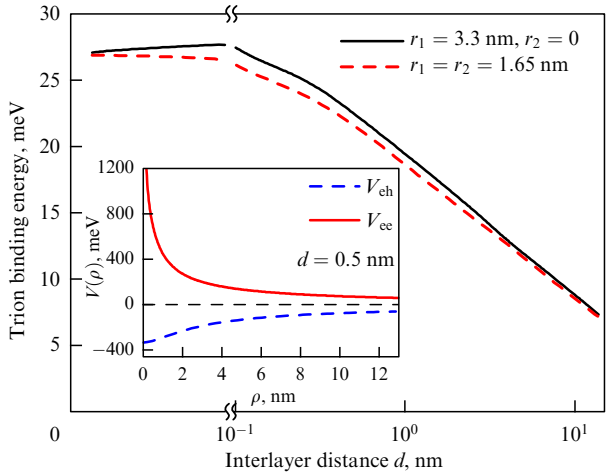

Figure 14. Trion binding energy as a function of the interlayer distance for $r_1 = 3.3$ nm and $r_2 = 0$ (solid curve) and $r_1 = r_2 = 1.65$ nm (dashed curve). Inset shows effective interaction potentials $V_{ee}(\rho)$ (solid line) and $V_{eh}(\rho)$ (dashed line) evaluated at $r_1 = r_2 = 1.65$ nm and $d = 0.5$ nm. Reduced mass is $\mu = 0.16m_0$, $m_e = m_h$ [81].

based on CdTe [154–156], GaAs [106, 107, 157–159], and ZnSe [160–162]) shows that the calculations done for ideal quantum wells give noticeably lower trion binding energies than the experiment (Fig. 15). The experimental results also depend more strongly on the width of the quantum well than predicted by theory. For narrow quantum wells, the discrepancy can reach two times [153]. A discrepancy between calculations and experiment is also observed for quantum wires [104].

The increase in the binding energy is explained by the localization of complexes on defects, which are inevitably contained in real structures. Such defects, for example, can be given by fluctuations in the width of quantum wells [163–167] and quantum wires [168–170], composition inhomogeneities [170–173], or fluctuations in the inherent charge distribution [174–177]. Such localized states of Coulomb complexes are in many respects similar to excitons and trions in quantum dots [178–187].

5.1 General method and the choice of a trial function

The problem of an electron–hole complex localized at the interface roughness was studied by the variational method using trial functions with a large (of the order of 10^4) number of fitting parameters or using the numerical diagonalization of the electron–hole Hamiltonian [50, 51], the method of path integrals [167], and the pseudopotential method [188]. As already noted, such calculations are best justified for specific structures with fixed parameters. Here, we discuss the more universal variational method in more detail, which, despite a reduction in accuracy, allows obtaining a lucid description of the structure and binding energy of a localized complex for arbitrary inhomogeneity parameters [189].

The influence of fluctuations in the quantum well width on charge carriers in narrow quantum wells can under certain conditions be reduced to the action of an additional potential in the quantum well plane [62]. The motion of charge carriers in the quantum well is considered to be two-dimensional. Let $U_e(\boldsymbol{\rho}_e)$ and $U_h(\boldsymbol{\rho}_h)$ be the effective two-dimensional inhomogeneity potentials acting on an electron and a hole. Fluctuations in the quantum wire radius are described similarly. The

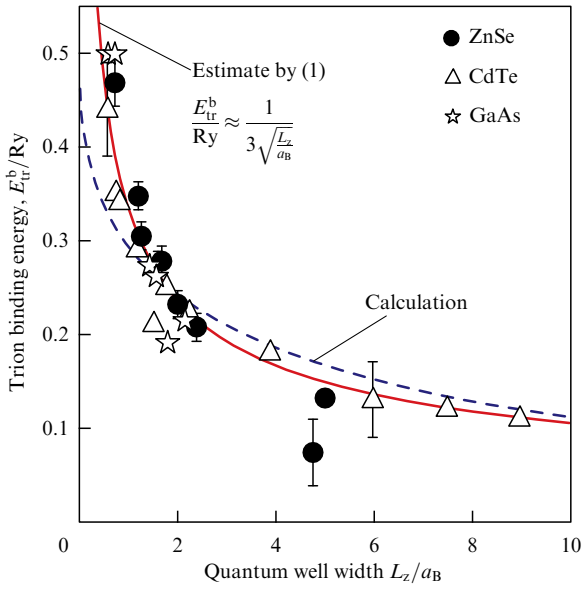

Figure 15. Dependence of the X^- trion binding energy on the quantum well width for different semiconductors, expressed in three-dimensional exciton Bohr units. Symbol: experimental data; solid line: phenomenological estimate; dashed line: calculation for the two-dimensional X^- trion at $m_e/m_h \to \infty$ [121].

ratios

$$W_e = \frac{\Delta E_e}{E_C}\,, \quad W_h = \frac{\Delta E_h}{E_C} \tag{22}$$

between E_C, which is a typical value of the inter-carrier Coulomb interaction, and ΔE_e and ΔE_h, which are the characteristic distances between the energy levels of noninteracting electrons and holes in the inhomogeneity potential, determine the general structure of the electron–hole complex. There are only two qualitatively different limit cases in which the Schrödinger equation can be simplified and reduced to several independent equations with fewer variables.

5.1.1 Limit case 1 ('weak' inhomogeneity potential). If the effective inhomogeneity potentials for both types of charge carriers are weak compared to the Coulomb interaction between them, $W_e, W_h \ll 1$, then the center-of-mass motion of the complex is slow compared to the relative motion of its component charge carriers, and in the adiabatic approximation its wave function can be represented as

$$\Psi(\mathbf{R}, \boldsymbol{\rho}_1, \ldots, \boldsymbol{\rho}_{N_e+N_h-1}) = \Psi^{CM}(\mathbf{R})\Psi^{int}(\boldsymbol{\rho}_1, \ldots, \boldsymbol{\rho}_{N_e+N_h-1})\,, \tag{23}$$

where $\mathbf{R}$ is the center-of-mass coordinate and $\boldsymbol{\rho}_i$ ($i = 1 \ldots N_e + N_h - 1$) are the relative coordinates of the particles in the complex. In this limit, the electron–hole complex is localized in the effective potential of the inhomogeneity as a whole, and the interaction with the inhomogeneity can be considered a perturbation. Here, N_e is the number of electrons, N_h is the number of holes, Ψ^{CM} is the envelope wave function of the center of mass of the electron–hole complex, and Ψ^{int} is the wave function of the relative motion of the charge carriers that make up the complex.

5.1.2 Limit case 2 ('strong' inhomogeneity potential). The second limit case is realized if the effective inhomogeneity potential for at least one type of charge carrier is strong compared to the Coulomb interaction. In other words, at least one of the conditions $W_e \gg 1$ and $W_h \gg 1$ is satisfied. Then, the coordinates of the electron and hole subsystems of the complex can be separated, because one of the subsystems is fast and the other is slow.

As a result, the wave function of the complex can be represented as

$$\Psi(\boldsymbol{\rho}_{e_1}, \ldots, \boldsymbol{\rho}_{e_{N_e}}, \boldsymbol{\rho}_{h_1}, \ldots, \boldsymbol{\rho}_{h_{N_h}}) = \Phi^{e}(\boldsymbol{\rho}_{e_1}, \ldots, \boldsymbol{\rho}_{e_{N_e}})\Phi^{h}(\boldsymbol{\rho}_{h_1}, \ldots, \boldsymbol{\rho}_{h_{N_h}})\,, \tag{24}$$

where $\Phi^{e(h)}(\boldsymbol{\rho}_{e(h)_1}, \ldots, \boldsymbol{\rho}_{e(h)_{N_{e(h)}}})$ is the wave function of the electron (hole) subsystem. Wave function (24) allows calculating the energy of the complex with an accuracy no worse than the first order of the perturbation theory, where the Coulomb interaction between electrons or holes is regarded as a perturbation.

In [189], a trial function was proposed that allows describing a smooth transition between functions (23) and (24) using a single fitting parameter, and thus combines limit cases 1 and 2:

$$\Psi(\boldsymbol{\rho}_{e_1}, \ldots, \boldsymbol{\rho}_{e_{N_e}}, \boldsymbol{\rho}_{h_1}, \ldots, \boldsymbol{\rho}_{h_{N_h}}) = \left[\Psi^{CM}(\mathbf{R})\Psi^{int}(\boldsymbol{\rho}_1, \ldots, \boldsymbol{\rho}_{N_e+N_h-1})\right]^{\alpha} \times \left[\Phi^{e}(\boldsymbol{\rho}_{e_1}, \ldots, \boldsymbol{\rho}_{e_{N_e}})\Phi^{h}(\boldsymbol{\rho}_{h_1}, \ldots, \boldsymbol{\rho}_{h_{N_h}})\right]^{1-\alpha}. \tag{25}$$

Here, α is a fitting parameter with the meaning of a correlation measure for the motion of charge carriers of various types: $\alpha = 1$ corresponds to limit case 1 and $\alpha = 0$ to limit case 2.

When the accuracy provided by trial function (25) is insufficient, a more complex trial function is proposed with two fitting parameters α and β,

$$\Psi(\boldsymbol{\rho}_{e_1}, \ldots, \boldsymbol{\rho}_{e_{N_e}}, \boldsymbol{\rho}_{h_1}, \ldots, \boldsymbol{\rho}_{h_{N_h}}) = \left[\Psi^{CM}(\mathbf{R})\Psi^{int}(\boldsymbol{\rho}_1, \ldots, \boldsymbol{\rho}_{N_e+N_h-1})\right]^{\alpha} \times \left[\Phi^{e}(\boldsymbol{\rho}_{e_1}, \ldots, \boldsymbol{\rho}_{e_{N_e}})\Phi^{h}(\boldsymbol{\rho}_{h_1}, \ldots, \boldsymbol{\rho}_{h_{N_h}})\right]^{\beta}, \tag{26}$$

and with four fitting parameters, α_e, α_h, α_ρ, and α_R,

$$\Psi(\boldsymbol{\rho}_{e_1}, \ldots, \boldsymbol{\rho}_{e_{N_e}}, \boldsymbol{\rho}_{h_1}, \ldots, \boldsymbol{\rho}_{h_{N_h}}) = \left[\Psi^{CM}(\mathbf{R})\right]^{\alpha_R}\left[\Psi^{int}(\boldsymbol{\rho}_1, \ldots, \boldsymbol{\rho}_{N_e+N_h-1})\right]^{\alpha_\rho} \times \left[\Phi^{e}(\boldsymbol{\rho}_{e_1}, \ldots, \boldsymbol{\rho}_{e_{N_e}})\right]^{\alpha_e}\left[\Phi^{h}(\boldsymbol{\rho}_{h_1}, \ldots, \boldsymbol{\rho}_{h_{N_h}})\right]^{\alpha_h}. \tag{27}$$

Although the functions Ψ^{CM}, Ψ^{int}, Φ^{e}, and Φ^{h} are not known in the general case, they are unchanged under the variational procedure and, for fixed parameters of the system, are to be calculated only once. These functions are solutions of decoupled Schrödinger equations for systems with fewer particles than the original system. Finding these functions is therefore a task of substantially lower complexity.

5.2 Binding energy of an exciton and trion localized on fluctuations of the width of quantum wells and quantum wires

The binding energies of excitons and trions localized on fluctuations of the width of quantum wells and of the radius of quantum wires with a parabolic effective potential were

calculated in [189–191]. Such a model can be used to describe the interface roughness of both quantum wells and quantum dots [192, 193]. The exciton binding energy was found to increase monotonically as the parameters W_e and W_h increase [189]. Estimates have shown that, for fluctuations in the width of a parabolic-potential quantum well, the error in calculating the exciton binding energy using the simplest one-parameter trial function (25) is about 10%, and the error in calculations with function (27) does not exceed 0.5%.

In [190], a variational method with trial function (27) with four fitting parameters was used to study the particular case of X^+ and X^- trions localized in the quantum well plane on a lateral parabolic potential. In Fig. 16, we show the calculated dependences of the binding energies of X^- and X^+ trions on the parameters W_e and W_h of the effective localizing potentials of the quantum well inhomogeneity, calculated at the mass ratio $\sigma = 0.3$. In contrast to the exciton binding energy, trion binding energies E_b^- and E_b^+ depend on the parameters W_e and W_h nonmonotonically, and the binding energies E_b^- and E_b^+ of negative and positive trions behave differently. As W_h increases, the binding energy of the X^- trion increases monotonically, while the binding energy of the X^+ trion decreases monotonically. For a fixed value of W_h, the dependence of E_b^- on W_e is nonmonotonic. This is because, with an increase in W_e, the efficiency of the exchange interaction between electrons increases, which first leads to an increase in the binding energy of the X^- trion. With a further increase in W_e, the contribution of the Coulomb repulsion between electrons dominates, and the binding energy decreases. In the case of an X^+ trion at a fixed value of W_e, the nonmonotonicity in the dependence of E_b^+ on W_h is not observed at $\sigma = 0.3$. This is explained by the larger mass of the hole and, accordingly, a reduced role of the exchange interaction.

The ratio between the binding energies of X^+ and X^- trions can be different; it depends on W_e and W_h. For example, if $W_e \gg \max(1, W_h)$, then E_b^- is greater than E_b^+; in the opposite limit, the binding energy of the X^- trion is higher. If the Coulomb repulsion between identical charge carriers cannot be compensated by the exchange interaction and attraction to the third charge carrier, then the trion binding energy can become negative. In limit cases, the accuracy of calculating the binding energies of X^+ and X^- trions by the variational method is estimated as 5 to 10%, and somewhat higher in the intermediate range [190].

For a GaAs quantum well structure, an increase in the well width by one monolayer in a region of radius 270 Å in the framework of variational calculations leads to an increase in the respective binding energy of the exciton and the X^+ and X^- trions by 5%, 15%, and 80% [190]. These values are somewhat smaller than those obtained in [51] for a similar inhomogeneity, but for a finite-width quantum well. The total increase in the binding energies of the exciton and the X^+ and X^- trions due to the localization of complexes was respectively obtained in [189] to be equal to 1.17, 0.44, and 1.67 meV. This differs from the results in [51] by 20 to 25% and is a good estimate in comparing the results of calculations for interface inhomogeneities of various shapes. The estimates made allow explaining the increase in the binding energy of the X^- trion observed experimentally (see [121] and references therein).

In [191], the binding energies of an exciton and X^+ and X^- trions localized at inhomogeneities of quantum wire interfaces were calculated similarly using a variational method. The nature of the dependences obtained largely

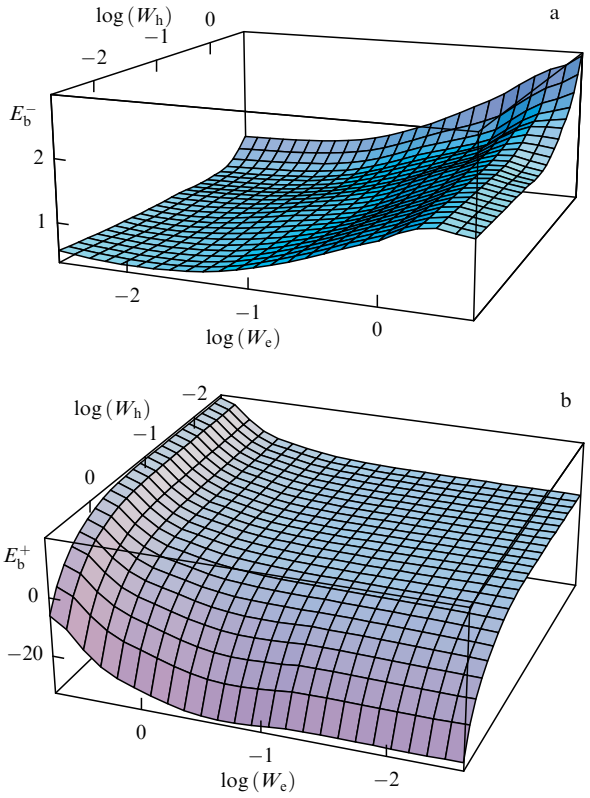

Figure 16. Binding energies of (a) X^- and (b) X^+ trions as functions of parameters W_e and W_h of the quantum well inhomogeneity potential, evaluated for electron and hole effective mass ratio $\sigma = 0.3$ [190].

reproduces the nature of the corresponding dependences for excitons and trions localized at inhomogeneities of quantum well interfaces [189, 190]. In such a system, the respective binding energies of the exciton and the X^- and X^+ trions increase by approximately 10%, 100%, and 40%, which is somewhat less than the values given in [104]. The increase in binding energies due to additional localization is about 2 and 0.9 meV for X^- and X^+ trions and differs from the corresponding values in [104] by 25%, which is good accuracy for such an estimate.

6. Accounting for valence band complexity. Effect of localization on the binding energy (via the example of an acceptor impurity)

In classical semiconductors such as GaAs or CdTe and similar ones, the conduction band is mainly formed by s-type atomic orbitals. The orbital part of the Bloch amplitude of the conduction band at the center of the Brillouin zone (the Γ point) is invariant. Taking spin into account, the states of a conduction electron at the center of the Brillouin zone are doubly degenerate, and as the absolute value of the quasiwave vector k increases, spin splitting arises in proportion to k^3 [62, 194, 195]. In contrast, the valence band is formed by p-type atomic orbitals. With spin taken into account, but without spin–orbit coupling, the states of the upper part of the valence band are sixfold degenerate, and taking the spin–orbit interaction into account leads to the splitting of states into a doublet and a quadruplet [62, 195–197], similarly to how the p-states of an atom split into states with the total angular momentum $J = 3/2$ and $J = 1/2$. In

crystals with a zinc blende lattice, which is characteristic of the most common semiconductor compounds, in particular, in III–V and II–VI systems, these states respectively transform under the irreducible Γ_8 and Γ_7 representations of the point group T_d (we here use the notation introduced in [198]).

In bulk materials, the effective mass of holes with angular momentum projections $\pm 3/2$ on the wave vector direction (a heavy-hole band) is typically much greater than that of states with projections $\pm 1/2$ (a light-hole band). The cubic symmetry of crystals manifests itself in the corrugation of the valence band, i.e., the dependence of the masses of holes on the direction of the wave vector and the absence of an inversion center manifest themselves in linear and cubic spin-dependent terms in the wave vector, which completely eliminate the degeneracy of hole states at $k \neq 0$ [199].

The spin–orbit splitting Δ of the valence band — the energy gap between the Γ_8 and Γ_7 subbands — is typically large and amounts to hundreds of meV. In studying Coulomb effects in bulk materials and nanostructures, in most cases, this allows considering the subbands Γ_8 and Γ_7 independently. The states of the Γ_8 subband are usually described in terms of the Luttinger Hamiltonian [62, 196, 200]

$$\mathcal{H}_{\rm L} = \frac{\hbar^2}{2m_0}\left[\left(1+\frac{5\gamma}{2}\right)k^2 - 2\gamma_2\sum_{\alpha}\{k_\alpha^2 J_\alpha^2\} - 2\gamma_3\sum_{\alpha\neq\beta}\{J_\alpha J_\beta\}k_\alpha k_\beta\right], \quad \alpha,\beta = x,y,z\,, \tag{28}$$

where γ_2 and γ_3 are the Luttinger parameters, J_α are the components of the operator of angular momentum 3/2, $\mathbf{k} = -\mathrm{i}\partial/\partial\mathbf{r}$ is the wave vector operator of the hole, $\mathbf{r}$ is the radius vector of the hole, and curly brackets denote the symmetrized product of operators: $\{J_\alpha J_\beta\} = (J_\alpha J_\beta + J_\beta J_\alpha)/2$.

The problems of size quantization of holes in quantum-well, quantum-wire, and quantum-dot structures, as well as the study of exciton effects, are made nontrivial by the matrix structure of the Hamiltonian. In a number of model cases, convenient analytic solutions have been found, in particular, for quantum-well structures with rectangular barriers and for spherically symmetric quantum-dot structures [201–204]. For Coulomb complexes, in particular, for acceptor-bound holes and excitons, the limit cases have been analyzed in detail, and a number of quite effective approximate methods are available [205–209]. In the general case, however, each specific problem requires a separate analysis.

The transition from bulk materials to lower-dimensional structures is typically accompanied by an increase in the interparticle interaction and in the binding energies of localized charge carriers and their complexes. But in systems with a complex band structure, size quantization can lead to a decrease in the binding energy of Coulomb complexes, e.g., for a neutral acceptor impurity (A^0), which is a complex consisting of a hole localized at a negatively charged center. Acceptor impurities largely determine the optical properties near the absorption edge in p-type structures in bulk materials [205, 206, 210–213] and quantum wells [214, 215].

Let us recall that, in the framework of the simple band model, the binding energies of a hydrogen-like complex in a bulk material, in an ideal two-dimensional quantum well, and in a small-radius quantum wire are [108, 216, 217]

$$E_{\rm b}^{\rm 3D} = \frac{e^4 m_{\rm 3D}}{2\hbar^2\varepsilon^2}\,, \tag{29a}$$

$$E_{\rm b}^{\rm 2D} = \frac{2e^4 m_{\rm 2D}}{\hbar^2\varepsilon^2}\,, \tag{29b}$$

$$E_{\rm b}^{\rm 1D} = \frac{2e^4 m_{\rm 1D}}{\hbar^2\varepsilon^2}\,\ln^2\left(\frac{a_{\rm B}}{R}\right), \tag{29c}$$

where $m_{\rm 3D}$, $m_{\rm 2D}$, and $m_{\rm 1D}$ are the effective masses in the bulk, in the quantum well plane, and along the quantum wire axis, R is the radius of the quantum wire, and $a_{\rm B} = \hbar^2\varepsilon/m_{\rm 1D}e^2$ is the effective Bohr radius.

It is generally accepted that, in passing from a bulk material to a low-dimensional structure, the binding energy of a hydrogen-like complex increases due to an increase in the efficiency of the Coulomb interaction [217]. For a hole in a complex valence band, the situation is more complicated. Localization typically leads to a decrease in the effective mass, which can in turn cause a decrease in the hole binding energy at the acceptor. In some cases, therefore, the acceptor binding energy can depend nonmonotonically on the size of the structure, and the acceptor binding energy in a narrow quantum well can decrease compared to the bulk material. Estimates by formulas (29a) and (29b) show that, for instance, the InAs parameters satisfy the relation $E_{\rm b}^{\rm 2D} < E_{\rm b}^{\rm 3D}$, showing that localization in a narrow quantum well compared with the size of the bulk acceptor leads to a decrease in the binding energy of the acceptor.

In [218], the binding energy of a hole on an acceptor was studied as regards its dependence on the quantum well width or on the quantum wire radius. Hole states belonging to the Γ_8 representation of the point group T_d (heavy and light holes) were considered. The boundary conditions do not include the terms that lead to the mixing of heavy and light holes in quantum wells with a sharp boundary at a zero wave vector of the hole in the well plane. Taking them into account does not result in qualitative and noticeable quantitative changes in the binding energies [219, 220], but is at the same time necessary for studying the fine structure of acceptor states. The band parameters and the dielectric constant are assumed to be the same in the entire space, and the acceptor is assumed to be located at the center of the quantum well or on the axis of the quantum wire.

The hole states are described in terms of the spherically symmetric approximation for the dimensionless Luttinger Hamiltonian (cf. (28) for $\gamma \equiv \gamma_2 = \gamma_3$):

$$\widehat{H} = \left(1+\frac{5\gamma}{2\gamma_1}\right)k^2 - \frac{2\gamma}{\gamma_1}\sum_{\alpha,\beta}\{k_\alpha k_\beta\}\{J_\alpha J_\beta\} - \frac{2}{r} + V_{\rm ext}(\mathbf{r})\,, \tag{30}$$

which also includes the Coulomb attraction of a hole to a charged center (the term $-2/r$) and the quantum well (wire) potential $V_{\rm ext}(\mathbf{r})$. The effective Rydberg radius $\mathrm{Ry}^* = m_0 e^4/2\gamma_1\varepsilon^2\hbar^2$ and the Bohr radius $a_{\rm B}^* = \hbar^2\gamma_1\varepsilon/m_0 e^2$, where m_0 is the free electron mass, are used as energy and length units. The acceptor binding energy was calculated within the variational method generalized to multicomponent wave functions; a rectangular potential with an infinite barrier and a parabolic potential were used as model heteropotentials of a quantum well (wire).

Localization in a quantum well starts noticeably affecting the acceptor structure when the well width becomes comparable to or smaller than the characteristic size $R_{\rm a}$ of the bulk acceptor wave function. In Fig. 17, we show the dependences

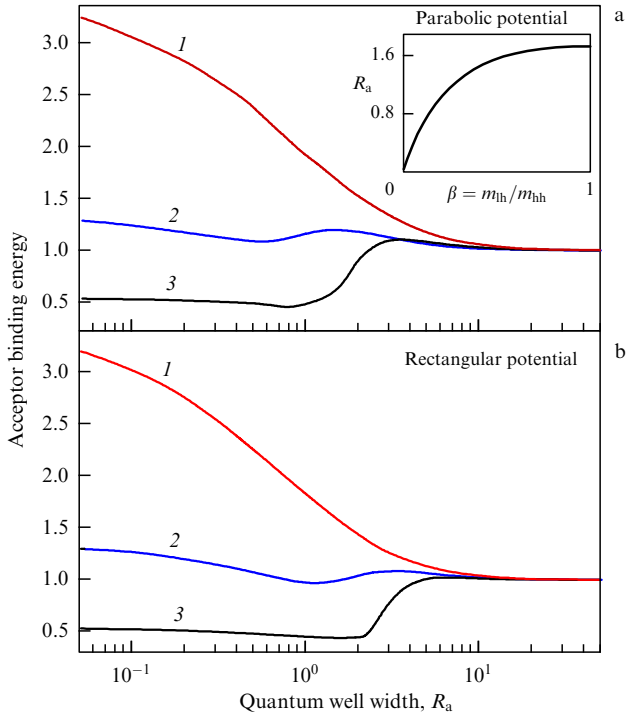

Figure 17. Acceptor binding energy (expressed in units of the energy of the bulk acceptor) as a function of the quantum well effective width for (a) a parabolic potential and (b) a rectangular potential with an infinite barrier. Curves *1–3* respectively correspond to different mass ratios of the light and heavy hole $\beta = m_{lh}/m_{hh}$: 0.67, 0.14, 0.052. Inset: dependence of R_a on β [218].

of the acceptor binding energy on the effective width of the quantum well calculated for different mass ratios of the heavy and light holes for quantum wells with a parabolic potential and a rectangular potential with an infinite barrier. The unit of energy was chosen as the energy of the bulk acceptor at a suitable ratio of the effective masses of light and heavy holes $\beta = (\gamma_1 - 2\gamma)/(\gamma_1 + 2\gamma)$. The characteristic size R_a of the bulk acceptor wave function at the same β was chosen as the unit of width for the well (see the inset to Fig. 17a).

At $\beta = (\gamma_1 - 2\gamma)/(\gamma_1 + 2\gamma)$ being sufficiently close to 1 (curves *1* in Fig. 17), the change in the effective mass of the hole due to its localization in the quantum well is small. The increase in the Coulomb interaction efficiency plays the leading role in changing the acceptor binding energy. In this case, the acceptor binding energy increases monotonically with a decrease in the effective width of the quantum well. As β decreases, the dependence of the acceptor binding energy on the quantum well width becomes nonmonotonic, which is related to a more significant change in the effective hole mass under the transition between the bulk material and the two-dimensional quantum well (curves *2*). The nonmonotonic behavior of the acceptor binding energy as a function of the effective quantum well width is expected to be most pronounced at small β (curves *3*).

The differences between the corresponding curves for the parabolic and rectangular potential models with an infinite barrier are very small in the limit cases. The differences are significant only directly in the region of the nonmonotonic dependence, which occurs at slightly different well widths, and are quantitative in nature. This indicates the universality of the dependences expressed in the same measurement units.

In [218], the dependence of the acceptor binding energy on the quantum wire radius was also studied. It was shown that a significant weakening of the nonmonotonicity is expected in the dependence of the acceptor binding energy on the quantum wire radius, compared to a similar dependence for quantum wells. This is due to the absence of a one-dimensional limit for the Coulomb interaction energy. Taking the corrugation of the valence band into account in [218] showed that the behavior of the binding energies is qualitatively similar to the dependences obtained in the spherical model: there are only quantitative differences, not exceeding 8% in the case of GaAs.

7. Trions in the Fermi sea of resident charge carriers

We have already mentioned that trions arise under excitation of low-dimensional semiconductor structures that contain free charge carriers (for definiteness, electrons) due to doping. In the presence of resident charge carriers, strictly speaking, the trion can no longer be regarded as an isolated complex [221]. This makes the problem of many-particle correlations in such a process relevant. Here, we present a relatively simple theoretical picture [52, 58] of the creation of trions and their manifestations in the optical properties of quantum wells containing electrons, with the correlation effects taken into account in the approximation of a low concentration of two-dimensional electrons n_e compared to the square of the reciprocal trion radius a_{tr}: $n_e a_{tr}^2 \ll 1$. We first list the relevant processes and explain them with diagrams: an exciton excited by an absorbed photon (Fig. 18a) either picks an electron from the Fermi sea of electrons and forms a trion (Fig. 18b) or is scattered on such electrons (Fig. 18c).

Using these three processes, we can construct a series for the susceptibility at frequencies close to the exciton transition frequency (Fig. 18d, where the exciton scattering amplitude T on quantum well electrons is shown with a dashed-dotted line). Here, $\Pi(\Omega)$ is the self-energy part and the photon energy Ω is referenced to the exciton creation energy. Near the exciton resonance, the first diagram is $\propto \Omega^{-1}$, and each next order of the diagrams adds the factor Ω^{-1}. The smallness of the diagrams of higher orders in the electron density is compensated by the smallness of Ω in the denominator, because all events occur near the exciton resonance. The scattering amplitude can be considered independent of the electron and exciton momenta if they are small compared to the inverse trion radius. The susceptibility then has the form

$$\chi_\uparrow = \chi_\downarrow = |D_{cv}|^2 \Psi^2(0) \times \left\{ \Omega + i\gamma - \int_0^F \left[\frac{1}{2} T_{sngl}\left(\Omega + \varepsilon\left(1 - \frac{m_e}{2m_e + m_h}\right)\right) + \frac{3}{2} T_{trpl}\left(\Omega + \varepsilon\left(1 - \frac{m_e}{2m_e + m_h}\right)\right)\right] d\varepsilon \right\}^{-1}, \quad (31)$$

where D_{cv} is the matrix element of the dipole interband transition, $\Psi(0)$ is the value of the wave function of the relative motion of an electron and a hole in the exciton at zero distance between them, $m_{e(h)}$ is the effective mass of the electron (hole), and γ is the radiative and nonradiative damping of the exciton. The arrows in the indices show the direction of the electron spin; T_{sngl} and T_{trpl} are the electron–exciton scattering amplitudes in the singlet and triplet states.

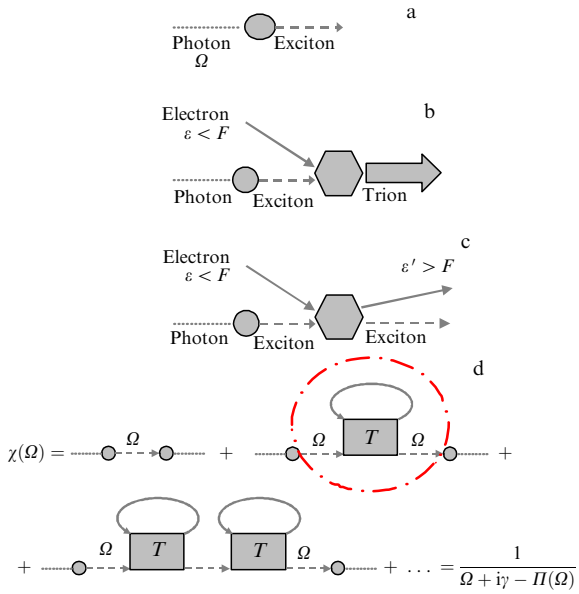

Figure 18. (a) Creation of an exciton by a quantum of light; (b) creation of a trion; (c) exciton scattering; (d) calculation of the susceptibility [52].

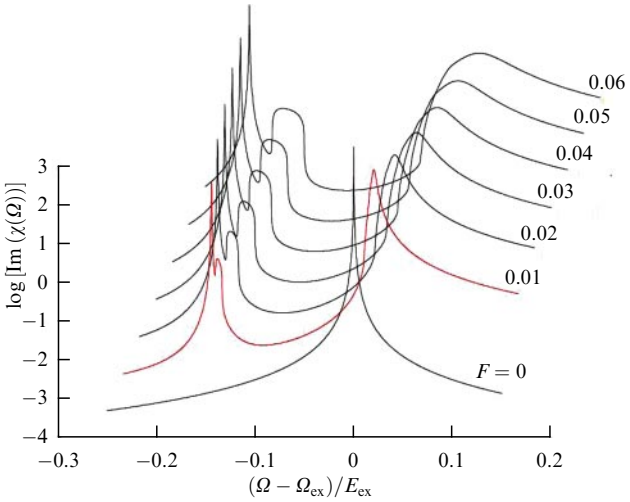

Figure 19. Dependence of the logarithm of the imaginary part of susceptibility (absorption) on photon energy Ω evolves as Fermi energy F increases from 0 to 0.06 (in units of E_{ex}^{b}), $E_{tr}^{b} = 0.15$, $m_h/m_e = 3$ [52].

The factors 1/2 and 3/2 take the statistical weight of these states into account, and the factors with mass ratios in brackets are responsible for the kinetic energies of the electron and the center of mass of the exciton.

The analysis is greatly simplified if we use the short-range nature of the interaction potential of an electron with excitons and the two-dimensional nature of their motion. Then, the scattering amplitudes can be represented as [52]

$$T_{sngl}(\Omega) = \frac{2\pi/\overline{m}}{\ln\left(E_{tr}^{b}/-\Omega\right)}\,, \quad T_{trpl}(\Omega) \approx \frac{2\pi/\overline{m}}{\ln\left(E_{exc}^{2}/(-\Omega E_1)\right)}\,, \tag{32}$$

where energy E_1 is of the order of the trion binding energy E_{tr}^{b} and $\overline{m}$ is the reduced mass of the exciton–electron pair. The singlet scattering amplitude $T_{sngl}(\Omega)$ has a pole corresponding to the 'bare' trion energy $-E_{tr}^{b}$. The scattering amplitude of the triplet has no pole in the region of interest to us. Susceptibility (31) has a pole at an energy less than $E_{tr}^{b} - F$. As the concentration of resident electrons increases, the exciton line broadens, and its tail propagates toward higher energies (Fig. 19). This broadening corresponds to processes in which an electron from under the Fermi surface is scattered into states with an energy greater than the Fermi one. Processes of this kind are responsible for the exciton–cyclotron resonance described in [222]. This 'tail' is then split into a series of levels separated from each other by the electron cyclotron frequency.

The processes described by the diagram in Fig. 18b lead, first, to a continuous absorption spectrum in the energy range from $-E_{tr}^{b} - F$ to $-E_{tr}^{b}$, and, second, to a delta-shaped peak corresponding to the bound state, whose nature is discussed below. The processes leading to the continuous spectrum (Fig. 18c) are of a simple nature. The photon gives rise to an exciton in the intermediate state, which picks up an electron from below the Fermi energy, forming a trion in the final state. The minimum energy required for this photon is $-E_{tr}^{b} - F$ when an electron with an energy equal to the Fermi energy is picked up, and the maximum corresponds to a zero-energy electron. The hole remaining in the Fermi sea after the escape of the electron to the trion does not couple to the photoproduced trion.

As regards the low-energy narrow delta peak in absorption, it is due to the creation of a trion–hole bound state in the Fermi sea of electrons. Its energy is found from the transcendental equation (whose derivation can be found in [52])

$$\frac{\Omega_{tetr}}{E_{tr}^{b}} = \ln\left(\frac{1 + \Omega_{tetr}/E_{tr}^{b} + E/E_{tr}^{b}}{1 + \Omega_{tetr}/E_{tr}^{b}}\right) = 0\,. \tag{33}$$

Equation (33) is valid only for $\Omega_{tetr} < -E_{tr}^{b} - F$: its solution for the susceptibility pole Ω_{tetr} as a function of the Fermi energy ratio to the binding energy of the trion is shown in Fig. 20.

It can be shown that for the eigenvalue Ω_{tetr} corresponding to the susceptibility pole, the wave function of the photocreated trion–hole pair in the Fermi sea oscillates with the period $1/k_F$ and decreases with the distance between the trion and the hole as $r^{-3/2}$ for $r > k_F^{-1}$ [52]. Thus, the wave function corresponding to the low-energy pole is normalizable to unity in two-dimensional space. This means that the hole in the Fermi sea is localized near the trion. Because we are in fact dealing with a complex of four quasiparticles (a hole in the valence band, two electrons entering the trion, and a hole in the Fermi sea), the authors of experimental work [223] called such a complex a 'tetron.' For Ω in the high-energy region, the wave function is complex: it oscillates and falls off with distance as $r^{-1/2}$ and is therefore not normalizable to unity. This corresponds to a hole in the Fermi sea escaping from the trion.

Thus, depending on the photon energy, there are two possibilities for trion photocreation in quantum wells with resident electrons:

(1) The production of a 'bare' trion and a hole in the Fermi sea that escaped from it. This process is characterized by a continuous absorption spectrum in the energy range

$$-E_{tr}^{b} - F < \Omega < -E_{tr}^{b}\,.$$

(2) Production of a pair made of a trion and a hole localized near it in the Fermi sea. The spectrum of this

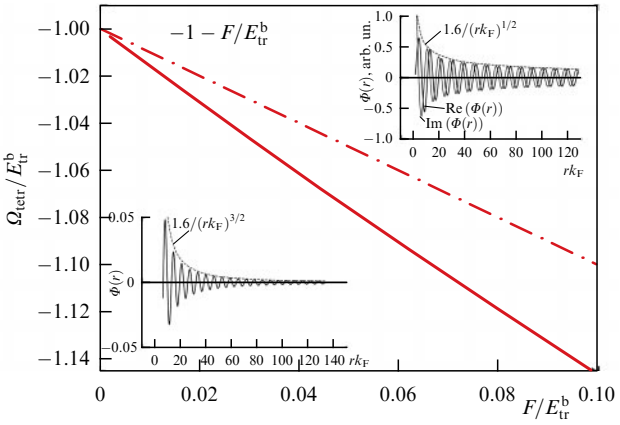

Figure 20. Dependence of tetron energy Ω_{tetr} on the Fermi energy (solid line). Dashed-dotted line shows the quantity $-1 - F/E_{tr}^{b}$. Insets: behavior of wave functions of the relative motion of a trion and a hole in the Fermi sea corresponding to a bound state and the state of a 'runaway' hole [52].

process is a delta function broadened due to scattering processes and a finite exciton lifetime due to radiative recombination.

A more detailed theory of the transition from an isolated trion to an exciton interacting with the Fermi sea of charge carriers was developed in [224]. The formation of a positive trion in the presence of a two-dimensional electron gas was studied numerically in [225]. In particular, the transition between the limits of the low electron gas concentration, when the trion can be regarded as an isolated complex, and the high concentration, when many-particle effects dominate, was studied. In [226], a review of theoretical approaches to the description of the interaction of an impurity with a two-dimensional Fermi gas is presented. In particular, it is shown that, if the mass of the impurity is finite, then it preserves the features of an isolated impurity in interacting with a Fermi gas, and we can speak of the formation of a new quasiparticle, a Fermi polaron. However, if the impurity mass is sufficiently large, then the perturbation of the Fermi sea is so strong that the resulting state becomes orthogonal to the state of the noninteracting impurity and loses the nature of a quasiparticle, because its mass vanishes (Anderson's orthogonality catastrophe [227]).

The concept of a Fermi polaron has undergone significant development in the physics of systems with extreme two-dimensionality, i.e., monolayers of transition-metal dichalcogenides [228–230]. The theory describes the corresponding experiment sufficiently well [228]. It was shown in [230] that both the many-particle approach (Fermi polaron) and the solution to the problem with a small number of particles (trion concept) lead to the same result at a sufficiently low concentration of resident charge carriers. In [230], a theory was also constructed for calculating the strength of the trion oscillator.

8. Conclusion

We have given a review of theoretical and partly experimental studies of Coulomb complexes such as neutral excitons and positive and negative trions in low-dimensional semiconducting systems: quantum wells, quantum wires, and monolayers of transition-metal dichalcogenides and van der Waals structures based on them. The described methods for analyzing the influence of Coulomb complexes on the electronic and optical properties of low-dimensional systems have been used to explain experimental results or to predict new effects.

We focused our attention on the variational methods that involve trial functions with a small number of fitting parameters endowed with a clear physical meaning. Such methods, first used by Bethe [10] and Chandrasekhar [67], while maintaining sufficient accuracy, allow following the changes in the binding energies and in the structure of the simplest electron–hole complexes with a change in the parameters of the system. The methods have shown their suitability for describing the localization of excitons and trions on the roughness of the interfaces of quantum wells and quantum wires, as well as for taking the complex structure of the valence band into account.

The results of studies of monolayers of transition-metal dichalcogenides and van der Waals heterostructures based on them, which involve a significant dielectric contrast, showed the viability of the macroscopic Rytova–Keldysh potential model [75, 76] for describing the interaction between charge carriers in such structures. The use of the Rytova–Keldysh potential allows describing the exciton series and obtaining reasonable values of the trion binding energy.

As we have demonstrated, the nonzero concentration of resident charge carriers must be taken into account in the description of Coulomb complexes in low-dimensional semiconducting structures. A lucid picture of the evolution of the spectra of structures with a change in the concentration of resident electrons and holes has been presented, and the role of correlation effects was analyzed.

This study was supported by the Russian Foundation for Basic Research project 19-12-50178 (Expansion).

References

1. Frenkel J *Phys. Rev.* **37** 17 (1931)
2. Frenkel J *Phys. Rev.* **37** 1276 (1931)
3. Wannier G H *Phys. Rev.* **52** 191 (1937)
4. Mott N F *Proc. R. Soc. Lond. A* **167** 384 (1938)
5. Gross E F, Karryev N A *Dokl. Akad. Nauk SSSR* **84** 261 (1952)
6. Knox R S *J. Phys. Chem. Solids* **9** 265 (1959)
7. Knox R S *Theory of Excitons* (Solid State Physics. Supplement 5) (New York: Academic Press, 1963)
8. Lampert M A *Phys. Rev. Lett.* **1** 450 (1958)
9. Urey H C *Phys. Rev.* **27** 216 (1926)
10. Bethe H *Z. Phys.* **57** 815 (1929)
11. Elkomoss S G, Amer A S *Phys. Rev. B* **11** 2925 (1975)
12. Stébé B, Munschy G *Solid State Commun.* **17** 1051 (1975)
13. Stébé B, Comte C *Phys. Rev. B* **15** 3967 (1977)
14. Combescot R *Phys. Rev. B* **100** 245201 (2019)
15. Kawabata T, Muro K, Narita S *Solid State Commun.* **23** 267 (1977)
16. Thomas G A, Rice T M *Solid State Commun.* **23** 359 (1977)
17. Stébé B et al. *Solid State Commun.* **26** 637 (1978)
18. Bastard G et al. *Phys. Rev. B* **26** 1974 (1982)
19. Schilling R, Mattis D C *Phys. Rev. Lett.* **49** 808 (1982)
20. Bobrysheva A I, Grodetskii M V, Zyukov V T *J. Phys. C* **16** 5723 (1983)
21. Stébé B, Ainane A *Superlatt. Microstruct.* **5** 545 (1989)
22. Kheng K et al. *Phys. Rev. Lett.* **71** 1752 (1993)
23. Finkelstein G, Shtrikman H, Bar-Joseph I *Phys. Rev. B* **53** R1709 (1996)
24. Brown J W, Spector H N *Phys. Rev. B* **35** 3009 (1987)
25. Degani M H, Hipólito O *Phys. Rev. B* **35** 9345 (1987)
26. Esser A, Zimmermann R, Runge E *Phys. Status Solidi B* **227** 317 (2001)
27. Tsuchiya T *Int. J. Mod. Phys. B* **15** 3985 (2001)
28. Otterburg T et al. *Phys. Rev. B* **71** 033301 (2005)

29. Akiyama H et al. *Solid State Commun*. **122** 169 (2002)
30. Ichida M et al. *Phys. Rev. B* **65** 241407 (2002)
31. Wang Z et al. *Phys. Rev. Lett*. **96** 047403 (2006)
32. Bulashevich K A, Suris R A, Rotkin S V *Int. J. Nanosci*. **2** 521 (2003)
33. Pedersen T G *Phys. Rev. B* **67** 073401 (2003)
34. Rønnow T F, Pedersen T G, Cornean H D *Phys. Rev. B* **81** 205446 (2010)
35. Grundmann M et al. *Phys. Rev. B* **53** R10509 (1996)
36. Wojs A, Hawrylak P *Phys. Rev. B* **51** 10880 (1995)
37. Hartmann A et al. *Phys. Rev. Lett*. **84** 5648 (2000)
38. Novoselov K S et al. *Science* **353** aac9439 (2016)
39. Geim A K, Grigorieva I V *Nature* **499** 419 (2013)
40. Mak K F et al. *Phys. Rev. Lett*. **105** 136805 (2010)
41. Splendiani A et al. *Nano Lett*. **10** 1271 (2010)
42. Wang Q H et al. *Nat. Nanotechnol*. **7** 699 (2012)
43. Mak K F, Shan J *Nat. Photon*. **10** 216 (2016)
44. Cadiz F et al. *Phys. Rev. X* **7** 021026 (2017)
45. Xiao D et al. *Phys. Rev. Lett*. **108** 196802 (2012)
46. Cao T et al. *Nat. Commun*. **3** 887 (2012)
47. Chernikov A et al. *Phys. Rev. Lett*. **113** 076802 (2014)
48. Wang G et al. *Rev. Mod. Phys*. **90** 021001 (2018)
49. Durnev M V, Glazov M M *Phys. Usp*. **61** 825 (2018); *Usp. Fiz. Nauk* **188** 913 (2018)
50. Dacal L C O et al. *Phys. Rev. B* **65** 115325 (2002)
51. Filinov A V et al. *Phys. Rev. B* **70** 035323 (2004)
52. Suris R A, in *Optical Properties of 2D Systems with Interacting Electrons* (NATO Science Series. Ser. II, Vol. 119, Eds W J Ossau, R Suris) (Dordrecht: Kluwer Acad. Publ., 2003) p. 111
53. Pines D *Elementary Excitations in Solids* (New York, Amsterdam: W.A. Benjamin, Inc., 1963); Translated into Russian: *Elementarnye Vozbuzhdeniya v Tverdykh Telakh* (Moscow: Mir, 1965)
54. Pikus F G *Sov. Phys. Semicond.* **26** 26 (1992); *Fiz. Tekh. Poluprovodn*. **26** 45 (1992)
55. Bigenwald P et al. *Phys. Rev. B* **61** 15621 (2000)
56. Bigenwald P et al. *Phys. Rev. B* **63** 035315 (2001)
57. Cox R T et al. *Phys. Rev. B* **69** 235303 (2004)
58. Suris R et al. *Phys. Status Solidi B* **227** 343 (2001)
59. Courtade E et al. *Phys. Rev. B* **96** 085302 (2017)
60. Mak K F et al. *Nat. Mater*. **12** 207 (2013)
61. Ross J S et al. *Nat. Commun*. **4** 1474 (2013)
62. Ivchenko E L *Optical Spectroscopy of Semiconductor Nanostructures* (Harrow: Alpha Science, 2005)
63. Reithmaier J-P, Höger R, Riechert H *Phys. Rev. B* **43** 4933 (1991)
64. Korobov V I *Phys. Rev. A* **61** 064503 (2000)
65. Bailey D H, Frolov A M *J. Phys. B* **35** 4287 (2002)
66. Karr J-Ph et al. *Can. J. Phys*. **85** 497 (2007)
67. Chandrasekhar S *Astrophys. J*. **100** 176 (1944)
68. Varga K, Suzuki Y *Phys. Rev. A* **53** 1907 (1996)
69. Thilagam A *Phys. Rev. B* **55** 7804 (1997)
70. Sergeev R A, Suris R A *Phys. Solid State* **43** 746 (2001); *Fiz. Tverd. Tela* **43** 714 (2001)
71. Hill R N *Phys. Rev. Lett*. **38** 643 (1977)
72. Larsen D M, McCann S Y *Phys. Rev. B* **45** 3485 (1992)
73. Sergeev R A, Suris R A *Phys. Status Solidi B* **227** 387 (2001)
74. Kormányos A et al. *2D Mater*. **2** 022001 (2015)
75. Rytova N S *Moscow Univ. Phys. Bull*. **22** (3) 18 (1967); *Vestn. Mosk. Univ. Ser. Fiz. Astron*. (3) 30 (1967)
76. Keldysh L V *JETP Lett*. **29** 658 (1979); *Pis'ma Zh. Eksp. Teor. Fiz*. **29** 716 (1979)
77. Keldysh L V *Phys. Status Solidi A* **164** 3 (1997)
78. Berkelbach T C, Hybertsen M S, Reichman D R *Phys. Rev. B* **88** 045318 (2013)
79. Kezerashvili R Ya, Tsiklauri S M *Few-Body Syst*. **58** 18 (2017)
80. Asriyan N A et al. *Phys. Rev. B* **99** 085108 (2019)
81. Semina M A *Phys. Solid State* **61** 2218 (2019); *Fiz. Tverd. Tela* **61** 2234 (2019)
82. Cudazzo P, Tokatly I V, Rubio A *Phys. Rev. B* **84** 085406 (2011)
83. Wu F, Qu F, MacDonald A H *Phys. Rev. B* **91** 075310 (2015)
84. Muljarov E A et al. *Phys. Rev. B* **51** 14370 (1995)
85. Glazov M M, Chernikov A *Phys. Status Solidi B* **255** 1800216 (2018)
86. Robert C et al. *Phys. Rev. Mater*. **2** 011001 (2018)
87. Fang H H et al. *Phys. Rev. Lett*. **123** 067401 (2019)
88. Wang G et al. *Phys. Rev. B* **90** 075413 (2014)
89. McCreary K M et al. *Sci. Rep*. **6** 35154 (2016)
90. Shang J et al. *ACS Nano* **9** 647 (2015)
91. Yu H et al. *Nat. Commun*. **5** 3876 (2014)
92. Borghardt S et al. *Phys. Rev. B* **101** 161402 (2020)
93. Cheiwchanchamnangij T, Lambrecht W R L *Phys. Rev. B* **85** 205302 (2012)
94. Van Tuan D, Yang M, Dery H *Phys. Rev. B* **98** 125308 (2018)
95. Szyniszewski M et al. *Phys. Rev. B* **95** 081301 (2017)
96. He K et al. *Phys. Rev. Lett*. **113** 026803 (2014)
97. Wang G et al. *Phys. Rev. Lett*. **114** 097403 (2015)
98. Larentis S et al. *Phys. Rev. B* **97** 201407 (2018)
99. Pisoni R et al. *Phys. Rev. Lett*. **121** 247701 (2018)
100. Glazov M M et al. *Phys. Rev. B* **100** 041301 (2019)
101. Arora A et al. *Phys. Rev. Lett*. **123** 167401 (2019)
102. Kośmider K, González J W, Fernández-Rossier J *Phys. Rev. B* **88** 245436 (2013)
103. Pikus G E, Averkiev N S *JETP Lett*. **34** 26 (1981); *Pis'ma Zh. Eksp. Teor. Fiz*. **34** 28 (1981)
104. Otterburg T et al. *Phys. Rev. B* **71** 033301 (2005)
105. Finkelstein G, Shtrikman H, Bar-Joseph I *Phys. Rev. Lett*. **74** 976 (1995)
106. Shields A J et al. *Phys. Rev. B* **51** 18049 (1995)
107. Finkelstein G, Shtrikman H, Bar-Joseph I *Phys. Rev. B* **53** R1709 (1996)
108. Loudon R *Am. J. Phys*. **27** 649 (1959)
109. Javanainen J, Eberly J H, Su Q *Phys. Rev. A* **38** 3430 (1988)
110. Su Q, Eberly J H, Javanainen J *Phys. Rev. Lett*. **64** 862 (1990)
111. Zhang F C, Das Sarma S *Phys. Rev. B* **33** 2903 (1986)
112. Jauregui K, Häusler W, Kramer B *Europhys. Lett*. **24** 581 (1993)
113. Schulz H J *Phys. Rev. Lett*. **71** 1864 (1993)
114. Fabrizio M, Gogolin A O, Scheidl S *Phys. Rev. Lett*. **72** 2235 (1994)
115. Egger R, Grabert H *Phys. Rev. B* **55** 9929 (1997)
116. Semina M A, Sergeev R A, Suris R A *Semiconductors* **42** 1427 (2008); *Fiz. Tekh. Poluprovodn*. **42** 1459 (2008)
117. Chaplik A V *Phys. Low-Dim. Struct*. **9/10** 131 (1999)
118. Szafran B et al. *Phys. Rev. B* **71** 235305 (2005)
119. Sidor Y, Partoens B, Peeters F M *Phys. Rev. B* **77** 205413 (2008)
120. Slachmuylders A F et al. *Phys. Rev. B* **76** 075405 (2007)
121. Sergeev R A et al. *Eur. Phys. J. B* **47** 541 (2005)
122. Dremin A A, Larionov A V, Timofeev V B *Phys. Solid State* **46** 170 (2004); *Fiz. Tverd. Tela* **46** 168 (2004)
123. Kukushkin I V et al. *Semicond. Sci. Technol*. **26** 014023 (2011)
124. Butov L V et al. *Phys. Rev. Lett*. **73** 304 (1994)
125. Lobanov S V, Gippius N A, Butov L V *Phys. Rev. B* **94** 245401 (2016)
126. Peeters F M, Golub J E *Phys. Rev. B* **43** 5159 (1991)
127. Dignam M M, Sipe J E *Phys. Rev. B* **43** 4084 (1991)
128. Bigenwald P, Gil B *Phys. Rev. B* **51** 9780 (1995)
129. Shields A J et al. *Phys. Rev. B* **55** 1318 (1997)
130. Kulakovskii D V, Lozovik Yu E *JETP Lett*. **76** 516 (2002); *Pis'ma Zh. Eksp. Teor. Fiz*. **76** 598 (2002)
131. Timofeev V B et al. *Phys. Rev. B* **60** 8897 (1999)
132. Sergeev R A, Suris R A *Semiconductors* **37** 1205 (2003); *Fiz. Tekh. Poluprovodn*. **37** 1235 (2003)
133. Semina M A, Suris R A *JETP Lett*. **94** 574 (2011); *Pis'ma Zh. Eksp. Teor. Fiz*. **94** 614 (2011)
134. Greene R L, Lane P *Phys. Rev. B* **34** 8639 (1986)
135. Blom A et al. *Phys. Rev. B* **65** 155302 (2002)
136. Fock V *Z. Phys*. **98** 145 (1935)
137. Pauli W (Jr.) *Z. Phys*. **36** 336 (1926)
138. Jauch J M, Hill E L *Phys. Rev*. **57** 641 (1940)
139. Parfitt D G W, Portnoi M E *J. Math. Phys*. **43** 4681 (2002)
140. Mota R D et al. *J. Phys. A* **35** 2979 (2002)
141. Calman E V et al. *Nat. Commun*. **9** 1895 (2018)
142. Jin C et al. *Nature* **567** 76 (2019)
143. Seyler K L et al. *Nature* **567** 66 (2019)
144. Tran K et al. *Nature* **567** 71 (2019)
145. Gerber I C et al. *Phys. Rev. B* **99** 035443 (2019)
146. Slobodeniuk A O et al. *2D Mater*. **6** 025026 (2019)
147. Bondarev I V *Mod. Phys. Lett. B* **30** 1630006 (2016)
148. Bondarev I V, Vladimirova M R *Phys. Rev. B* **97** 165419 (2018)
149. Berman O L, Kezerashvili R Ya *Phys. Rev. B* **96** 094502 (2017)

150. Brunetti M N, Berman O L, Kezerashvili R Ya *J. Phys. Condens. Matter* **30** 225001 (2018)
151. Kezerashvili R Ya, Spiridonova A *Phys. Rev. Res.* **3** 033078 (2021)
152. Riva C, Peeters F M, Varga K *Phys. Rev. B* **61** 13873 (2000)
153. Peeters F M, Riva C, Varga K *Physica B* **300** 139 (2001)
154. Wojtowicz G K T, Kutrowski M, Kossut J *Acta Phys. Polon. A* **94** 199 (1998)
155. Huard V et al. *Phys. Rev. Lett.* **84** 187 (2000)
156. Kochereshko V P et al. *Phys. Status Solidi B* **221** 345 (2000)
157. Yan Z C et al. *Phys. Rev. B* **52** 5907 (1995)
158. Kaur R et al. *Phys. Status Solidi A* **178** 465 (2000)
159. Esser A et al. *Phys. Rev. B* **62** 8232 (2000)
160. Kheng K, Saminadayar K, Magnea N *J. Crystal Growth* **184 – 185** 849 (1998)
161. Homburg O et al. *Phys. Rev. B* **62** 7413 (2000)
162. Astakhov G V et al. *Phys. Rev. B* **65** 165335 (2002)
163. Petroff P M *J. Vac. Sci. Technol.* **14** 973 (1977)
164. Weisbuch C et al. *J. Vac. Sci. Technol.* **17** 1128 (1980)
165. Bastard G et al. *Phys. Rev. B* **29** 7042 (1984)
166. Delalande C, Meynadier M H, Voos M *Phys. Rev. B* **31** 2497 (1985)
167. Bracker A S et al. *Phys. Rev. B* **72** 035332 (2005)
168. Thornton T J et al. *Phys. Rev. Lett.* **63** 2128 (1989)
169. Notomi M, Okamoto M, Tamamura T *J. Appl. Phys.* **75** 4161 (1994)
170. Quang D N, Tung N H *Phys. Rev. B* **62** 15337 (2000)
171. Baranovskii S D, Efros A L *Sov. Phys. Semicond.* **12** 1328 (1978); *Fiz. Tekh. Poluprovodn.* **12** 2233 (1978)
172. Baranovskii S D et al. *Phys. Rev. B* **48** 17149 (1993)
173. Litvinov V I, Razeghi M *Phys. Rev. B* **59** 9783 (1999)
174. Bryant G W *Phys. Rev. B* **29** 6632 (1984)
175. Brown J W, Spector H N *J. Appl. Phys.* **59** 1179 (1986)
176. Bastard G *Phys. Rev. B* **24** 4714 (1981)
177. Harris C I et al. *Phys. Rev. B* **51** 13221 (1995)
178. Kulakovskii V D, Butov L V *Phys. Usp.* **38** 219 (1995); *Usp. Fiz. Nauk* **165** 229 (1995)
179. Hawrylak P, Wojs A *Semicond. Sci. Technol.* **11** 1516 (1996)
180. Hawrylak P *Phys. Rev. B* **60** 5597 (1999)
181. Bacher G et al. *Phys. Rev. Lett.* **83** 4417 (1999)
182. Bimberg D, Grundmann M, Ledenstov N N *Quantum Dot Heterostructures* (New York: Wiley, 1999)
183. Bayer M et al. *Phys. Rev. B* **65** 195315 (2002)
184. Urbaszek B et al. *Phys. Rev. Lett.* **90** 247403 (2003)
185. Karrai K et al. *Nature* **427** 135 (2004)
186. Durnev M V et al. *Phys. Rev. B* **87** 085315 (2013)
187. Durnev M V et al. *Phys. Rev. B* **93** 245412 (2016)
188. Luo J-W, Bester G, Zunger A *Phys. Rev. B* **79** 125329 (2009)
189. Semina M A, Sergeev R A, Suris R A *Semiconductors* **40** 1338 (2006); *Fiz. Tekh. Poluprovodn.* **40** 1373 (2006)
190. Semina M A, Sergeev R A, Suris R A *Physica E* **40** 1357 (2008)
191. Semina M A, Sergeev R A, Suris R A *Semiconductors* **43** 1182 (2009); *Fiz. Tekh. Poluprovodn.* **43** 1222 (2009)
192. Gevorkyan G S, Lozovik Yu E *Sov. Phys. Solid State* **27** 1079 (1985); *Fiz. Tverd. Tela* **27** 1800 (1985)
193. Que W *Phys. Rev. B* **45** 11036 (1992)
194. Dresselhaus G *Phys. Rev.* **100** 580 (1955)
195. Dyakonov M I (Ed.) *Spin Physics in Semiconductors* (Springer Series in Solid-State Sciences, Vol. 157) 2nd ed. (Berlin: Springer, 2017)
196. Luttinger J M, Kohn W *Phys. Rev.* **97** 869 (1955)
197. Dresselhaus G, Kip A F, Kittel C *Phys. Rev.* **98** 368 (1955)
198. Koster G F et al. *Properties of the Thirty-Two Point Groups* (M.I.T. Press Research Monographs, No. 34) (Cambridge, MA: M.I.T. Press, 1963)
199. Pikus G E, Marushchak V A, Titkov A N *Sov. Phys. Semicond.* **22** 115 (1988); *Fiz. Tekh. Poluprovodn.* **22** 185 (1988)
200. Luttinger J M *Phys. Rev.* **102** 1030 (1956)
201. Nedorezov S S *Sov. Phys. Solid State* **12** 1814 (1971); *Fiz. Tverd. Tela* **12** 2269 (1970)
202. Broido D A, Sham L J *Phys. Rev. B* **31** 888 (1985)
203. Efros Al L et al. *Phys. Rev. B* **54** 4843 (1996)
204. Gupalov S V, Ivchenko E L *Phys. Solid State* **42** 2030 (2000); *Fiz. Tverd. Tela* **42** 1976 (2000)
205. Baldereschi A, Lipari N *Phys. Rev. B* **8** 2697 (1973)
206. Baldereschi A, Lipari N O *Phys. Rev. B* **9** 1525 (1974)
207. Gel'mont B L, D'yakonov M I *Sov. Phys. Semicond.* **5** 1905 (1972); *Fiz. Tekh. Poluprovodn.* **5** 2191 (1971)
208. Gel'mont B L, D'yakonov M I *Sov. Phys. Semicond.* **7** 1345 (1973); *Fiz. Tekh. Poluprovodn.* **7** 2013 (1973)
209. Kane E O *Phys. Rev. B* **11** 3850 (1975)
210. Kohn W, Schechter D *Phys. Rev.* **99** 1903 (1955)
211. Kogan Sh M, Polupanov A F *Sov. Phys. JETP* **53** 201 (1981); *Zh. Eksp. Teor. Fiz.* **80** 394 (1981)
212. Averkiev N S, Rodina A V *Sov. Phys. Solid State* **35** 538 (1993); *Fiz. Tverd. Tela* **35** 1051 (1993)
213. Merkulov I A, Rodina A V *Semiconductors* **28** 195 (1994); *Fiz. Tekh. Poluprovodn.* **28** 321 (1994)
214. Miller R C et al. *Phys. Rev. B* **25** 3871 (1982)
215. Zhao Q X et al. *Phys. Rev. B* **63** 195317 (2001)
216. Davies J H *The Physics of Low-Dimensional Semiconductors: An Introduction* (Cambridge: Cambridge Univ. Press, 1998)
217. Ivchenko E L, Pikus G E *Superlattices and Other Heterostructures: Symmetry and Optical Phenomena* (Berlin: Springer, 1997)
218. Semina M A, Suris R A *Semiconductors* **45** 917 (2011); *Fiz. Tekh. Poluprovodn.* **45** 947 (2011)
219. Aleiner I L, Ivchenko E L *JETP Lett.* **55** 692 (1992); *Pis'ma Zh. Eksp. Teor. Fiz.* **55** 662 (1992)
220. Ivchenko E L, Kaminski A Yu, Rössler U *Phys. Rev. B* **54** 5852 (1996)
221. Hawrylak P *Phys. Rev. B* **44** 3821 (1991)
222. Yakovlev D R et al. *Phys. Rev. Lett.* **79** 3974 (1997)
223. Koudinov A V et al. *Phys. Rev. Lett.* **112** 147402 (2014)
224. Chang Y-C, Shiau S-Y, Combescot M *Phys. Rev. B* **98** 235203 (2018)
225. Spink G G et al. *Phys. Rev. B* **94** 041410 (2016)
226. Schmidt R et al. *Rep. Prog. Phys.* **81** 024401 (2018)
227. Anderson P W *Phys. Rev. Lett.* **18** 1049 (1967)
228. Sidler M et al. *Nat. Phys.* **13** 255 (2017)
229. Efimkin D K, MacDonald A H *Phys. Rev. B* **95** 035417 (2017)
230. Glazov M M *J. Chem. Phys.* **153** 034703 (2020)